Exploring reverse silicate weathering across geological time: a review

Andre Baldermann[1]*, Santanu Banerjee[2], Stefan C. Löhr[3], Maxim Rudmin[4], Laurence N. Warr[5] and Arpita Chakraborty[2]

[1]*Institute of Applied Geosciences, Graz University of Technology and NAWI Graz Geocenter, Graz, Austria*

[2]*Department of Earth Sciences, Indian Institute of Technology Bombay, Powai, Mumbai, India*

[3]*Department of Earth Sciences, University of Adelaide, Engineering North, North Terrace Campus, Adelaide, SA, Australia*

[4]*Division for Geology, School of Earth Sciences & Engineering, Tomsk Polytechnic University, Tomsk, Russia*

[5]*Institute of Geography and Geology, University of Greifswald, Greifswald, Germany*

*Email: baldermann@tugraz.at

Running head: Reverse silicate weathering across geological time
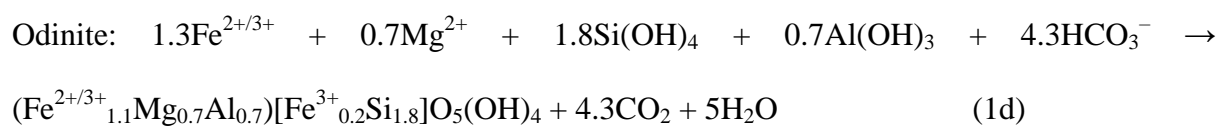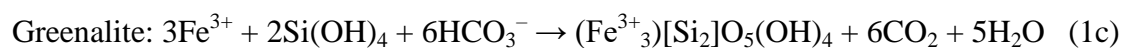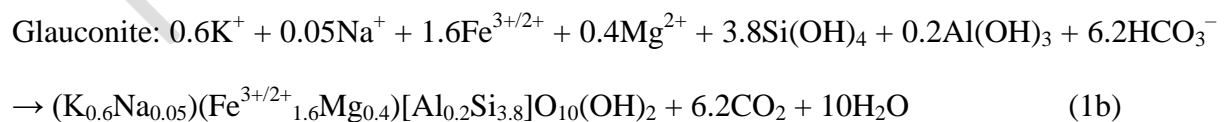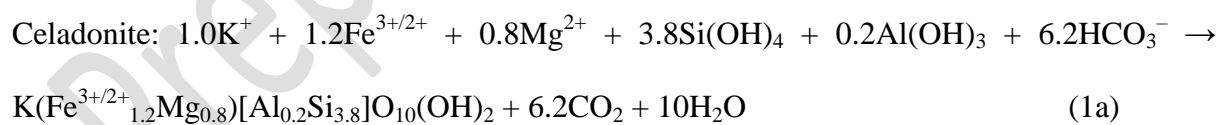
Abstract

Marine clay mineral authigenesis, referred to as reverse (silicate) weathering, is one of the first-order controls on seawater pH through the generation of acidity and thus plays a significant role in controlling carbon cycling between marine sediments, oceans and the
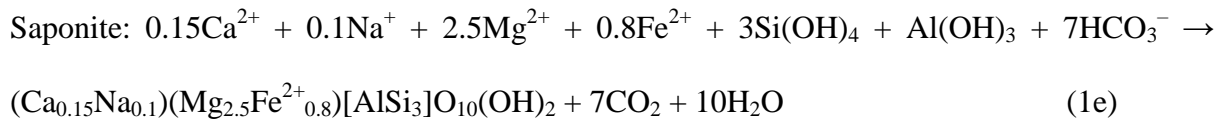
atmosphere over geological timescales. Reverse weathering is mainly regulated by the rates of silicate and carbonate weathering on the continents, the reactivity of detritus supplied to the oceans and the rates of seafloor weathering. These processes provide essential dissolved components (e.g. K^+, Mg^{2+}, Ca^{2+}, $Si(OH)_4$, Al^{3+}, $Fe^{2+/3+}$) to the marine porewater inventory that cause authigenic clay minerals, such as odinite, glauconite, celadonite and greenalite, to form close to the sediment–seawater interface. Such clay mineral reactions impact the sedimentary cycling *versus* sequestration of chemical elements, importantly Si, Fe, Mg and K, and consequently contribute to the fluctuations in climate and seawater composition recorded in marine archives over geological time. This review explores the links between reverse silicate weathering and the climate system across geological timescales and provides estimates of the elemental uptake fluxes associated with modern-day clay mineral authigenesis. Novel isotope proxies (e.g. $\delta^{41}K$ and $\delta^{30}Si$) and promising new dating techniques (e.g. *in situ* Rb/Sr geochronology) provide improved constraints on the timing, kinetics and environmental significance of clay mineral reactions on the ocean floor. We also consider recent geoengineering developments linked to reverse weathering reactions, such as ongoing attempts to reduce atmospheric CO_2 concentrations *via* marine alkalinity enhancement and the application of marine clay mineral-based slow-release fertilizers to soils to optimize nutrient availability.

Retrograde clay mineral formation on the ocean floor, also called reverse weathering, has strongly influenced the mineralogical and biogeochemical composition of Earth's marine sediments, the chemistry of its seawater and the composition of its atmosphere across geological time (Mackenzie & Garrels, 1966a, 1966b; Mackin & Aller, 1984; Siever, 1992;

Mackenzie & Kump, 1995; Michalopoulos & Aller, 1995; Misra & Froehlich, 2012; Isson & Planavsky, 2018; Li *et al.*, 2021a; Baldermann *et al.*, 2022; Rauzi *et al.*, 2024). In this process, porewater- or seawater-derived $Si(OH)_4$ reacts with HCO_3^- ions, dissolved cations and metal aquo-complexes, such as $Fe^{2+/3+}$, Mg^{2+}, K^+, Na^+, Ca^{2+} and $Al(OH)_3^0$, to form a suite of authigenic clay minerals, as well as variable amounts of acidity (H^+) during early marine diagenesis (e.g. Siever, 1992; Michalopoulos *et al.*, 2000; Hazen *et al.*, 2013; Tosca *et al.*, 2016; Cuadros *et al.*, 2017; Frings, 2017; Cao *et al.*, 2022; Ma *et al.*, 2022; Steiner *et al.*, 2022; Wallmann *et al.*, 2023). As a result, near-surface clay mineral authigenesis impacts the evolution of seawater pH and the marine element cycles, and potentially serves as a long-term regulator of Earth's climate by influencing atmospheric CO_2 concentrations (e.g. Kump *et al.*, 2000; Isson & Planavsky, 2018; Andrews *et al.*, 2020; Isson *et al.*, 2020; Krissansen-Totton & Catling, 2020; Li *et al.*, 2021a; Warr, 2022; Yin *et al.*, 2023). Reverse weathering reactions have been documented in a diverse range of marine settings, including 'low'-temperature shallow shelf and deep-marine environments, as well as 'high'-temperature (up to a few hundred °C) settings associated with mid-oceanic ridge sites, or transform faults. Common examples of clay mineral precipitation reactions are given in Equation 1a–e (modified after Isson & Planavsky, 2018):

Celadonite: $1.0K^+ + 1.2Fe^{3+/2+} + 0.8Mg^{2+} + 3.8Si(OH)_4 + 0.2Al(OH)_3 + 6.2HCO_3^- \rightarrow$
$K(Fe^{3+/2+}_{1.2}Mg_{0.8})[Al_{0.2}Si_{3.8}]O_{10}(OH)_2 + 6.2CO_2 + 10H_2O$ (1a)

Glauconite: $0.6K^+ + 0.05Na^+ + 1.6Fe^{3+/2+} + 0.4Mg^{2+} + 3.8Si(OH)_4 + 0.2Al(OH)_3 + 6.2HCO_3^-$
$\rightarrow (K_{0.6}Na_{0.05})(Fe^{3+/2+}_{1.6}Mg_{0.4})[Al_{0.2}Si_{3.8}]O_{10}(OH)_2 + 6.2CO_2 + 10H_2O$ (1b)

Greenalite: $3Fe^{3+} + 2Si(OH)_4 + 6HCO_3^- \rightarrow (Fe^{3+}_3)[Si_2]O_5(OH)_4 + 6CO_2 + 5H_2O$ (1c)

Odinite: $1.3Fe^{2+/3+} + 0.7Mg^{2+} + 1.8Si(OH)_4 + 0.7Al(OH)_3 + 4.3HCO_3^- \rightarrow$
$(Fe^{2+/3+}_{1.1}Mg_{0.7}Al_{0.7})[Fe^{3+}_{0.2}Si_{1.8}]O_5(OH)_4 + 4.3CO_2 + 5H_2O$ (1d)

Saponite: $0.15Ca^{2+} + 0.1Na^{+} + 2.5Mg^{2+} + 0.8Fe^{2+} + 3Si(OH)_4 + Al(OH)_3 + 7HCO_3^{-} \rightarrow$

$(Ca_{0.15}Na_{0.1})(Mg_{2.5}Fe^{2+}_{0.8})[AlSi_3]O_{10}(OH)_2 + 7CO_2 + 10H_2O$ (1e)

Many of these authigenic marine clay minerals are Fe-rich, have a greenish colour and show a high but temporally restricted abundance in the rock record. Some of them even form distinct facies, such as the well-known glaucony and verdine facies (e.g. Rubio & López-Pérez, 2024). These unique Fe-rich clay minerals preferentially precipitate in semi-confined geochemical micro-environments, such as in faecal pellets or foraminifera chambers, within marine sedimentary sequences that cover large areas of modern shelf and deep-sea areas and characterized equivalent ancient environments (e.g. Odin, 1988; Baldermann *et al.*, 2012, 2022; Banerjee *et al.*, 2015, 2016).

In the geological record, the occurrence of large deposits of authigenic marine clay minerals, such as ironstones and greensands, is often found to be associated with high rates of bio-opal remineralization (Michalopoulos & Aller, 2004). This relationship suggests a close linkage between the global silica and other element cycles – importantly, C, K, Mg and Fe (e.g. Pogge von Strandmann *et al.*, 2013; Dunlea *et al.*, 2017; Baldermann *et al.*, 2022; Isson & Rauzi, 2024). However, quantifying the role of reverse weathering in global biogeochemical cycles and the climate system remains difficult because the mechanisms and rates of individual reactions are often not known (e.g. Ehlert *et al.*, 2016; Rahman *et al.*, 2016; Krissansen-Totton & Catling, 2020). Nevertheless, there is ample evidence that marine clay mineral authigenesis has had a strong effect on Earth's climatic evolution and the marine sedimentary element cycles – relationships that are discussed in this article. Moreover, this article reviews the temporal distribution and abundance of authigenic clay minerals in marine sedimentary archives from the Precambrian to recent epochs by focusing on the formation of beidellite, berthierine, chamosite, celadonite, glauconite, greenalite, kaolinite, minnesotaite, odinite, palygorskite, saponite, sepiolite, stevensite, stilpnomelane, talc and vermiculite (Fig.

1). Recent advances in trace element and isotope geochemistry of authigenic clay minerals are also presented, and examples are provided highlighting the importance of clay mineral formation *versus* weathering in marine geoengineering and in slow-release fertilizer technology.
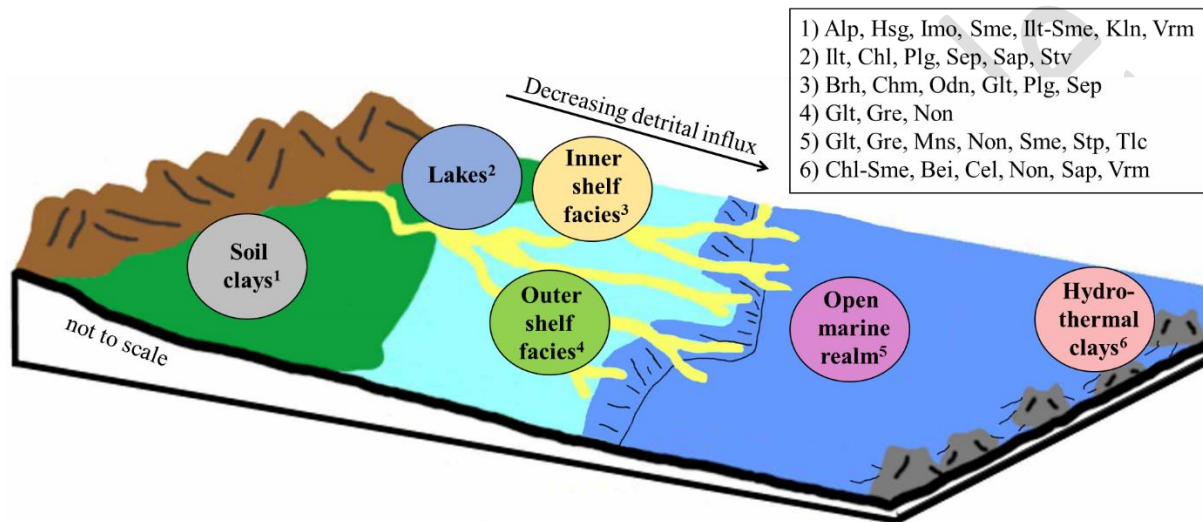

Figure 1. Illustration showing selected sedimentary environments characterized by authigenic clay mineral formation. Common clay mineral assemblages forming in each depocentre are indicated at the top right. The yellow meandering strands indicate deltas and subaquatic channels. International Mineralogical Association (IMA)-approved clay minerals abbreviations after Warr (2020): Alp = allophane; Bei = beidellite; Brh = berthierine; Cel = celadonite; Chl = chlorite; Chl-Sme = chlorite-smectite; Chm = chamosite; Glt = glauconite; Gre = greenalite; Hsg = hisingerite; Ilt = illite; Ilt-Sme = illite-smectite; Imo = imogolite; Kln = kaolinite; Mns = minnesotaite; Non = nontronite; Odn = odinite; Plg = palygorskite; Sap = saponite; Sep = sepiolite; Sme = smectite; Stp = stilpnomelane; Stv = stevensite; Tlc = talc; Vrm = vermiculite.

Reverse weathering scenarios and climate evolution across geological time

Weathering, erosion and biodegradation are the main mechanisms that cause the breakdown of rocks and minerals on Earth's surface. These processes trigger congruent and incongruent dissolution of primary siliceous, calcareous and other minerals, providing dissolved elements, colloids, degraded minerals and solid matter to rivers, groundwaters and surface waters, which ultimately enter the oceans (Fig. 2). Thus, by regulating supply, weathering reactions on the continents play a central role in controlling ocean (bio)geochemical reactions at the sediment–seawater interface and in the marine element cycle(s) through time (e.g. Singer, 1980, 1984; Michalopoulos & Aller, 1995; Isson & Planavsky, 2018; Isson *et al.*, 2020; Kalderon-Asal *et al.*, 2021).

Silicate minerals compose over 90% of the rocks found in Earth's near-surface environments. As most of them are unstable under ambient pressure and temperature conditions, they are susceptible to various forms of physical alteration and chemical degradation (e.g. Wilson, 1999, 2004). The incongruent dissolution of primary igneous silicate minerals, such as olivine, pyroxene, amphibole, feldspar and mica, and the resulting supply of cations are therefore often viewed as prerequisites for the formation of secondary clay minerals in the critical zone (i.e. soils) and in the widespread marine realm (e.g. Banfield *et al.*, 1991; Wilson, 1999, 2004; Gillis & Coogan, 2011; Rafiei *et al.*, 2020). These reactions are ultimately linked to regulating Earth's climate and its carbon cycle over the long term. There are various numerical models available (reviewed by Penman *et al.*, 2020) that aim at understanding and quantifying (at least parts of) the complex feedback mechanisms and rates between silicate weathering, reverse weathering and climate change. These consider changes in parameters through geological time, such as the partial pressure of CO_2 in the atmosphere (pCO_2), the rates of continental and seafloor weathering and erosion (e.g. Coogan & Gillis, 2013, 2018, 2020), vegetational cover, topography and temperature, among other factors (e.g.

Penman *et al.*, 2020). The key parameters controlling climate change and the palaeoclimatic evolution of Earth remain, however, focuses of continued debate. This reflects the complexity of quantifying silicate dissolution (CO_2 sink) *versus* clay mineral formation processes (CO_2 source) occurring in Earth's broad spectrum of near-surface environments and the resulting limitations in modelling and predicting global elemental fluxes and their sensitivity to climate (e.g. Keller & Wood, 1993; Isson *et al.*, 2020; Krissansen-Totton & Catling, 2020). On geological timescales, silicate weathering and clay mineral cycles are also linked to plate tectonic processes, with faster subduction cycles occurring along active plate margins and slower cycles taking place on passive continental margins (reviewed by Warr, 2022). This means that there is an intimate relationship between silicate weathering, clay mineral precipitation, climate and the tectono-thermal behaviour of the lithosphere.
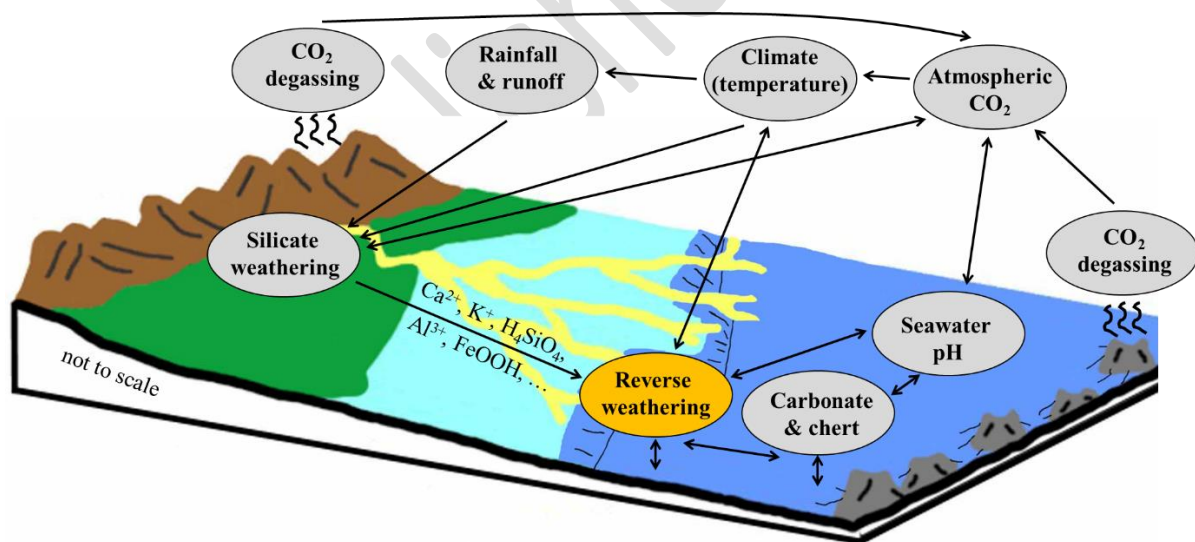
Figure 2. Illustration showing the complex interplay between terrestrial (silicate) weathering, marine bioproductivity, reverse weathering reactions, ocean biogeochemistry and atmospheric circulation, which all contribute to Earth's climatic evolution (after Isson & Planavsky, 2018). The yellow meandering strands indicate deltas and subaquatic channels.

It is well-established that Earth's early climate was characterized by warmth and stability, with ice-free conditions prevailing during most of the Proterozoic eon (2,500–541 Myr ago), except for the extreme glaciation events in the Cryogenian (e.g. Lipp *et al.*, 2021; Isson & Rauzi, 2024). This occurred despite the solar luminosity being ~5–20% lower than in the present day (e.g. Gough, 1981). The long-lasting climate stability changed dramatically in the Phanerozoic eon (541 Myr–present), with the appearance of frequent and rapid icehouse–greenhouse cycles (e.g. Royer *et al.*, 2004). The reasons for this climate transition have been controversially discussed in the literature. Proposed explanations include temporal changes in Earth's crustal composition (e.g. Gaillardet *et al.*, 1999; Coogan & Dosso, 2015), increased uplift and erosional rates, as well as changes in ocean currents (e.g. Foster & Rohling, 2013), which had maintained elevated pCO_2 during the Precambrian (e.g. Kump *et al.*, 2000; Isson & Planavsky, 2018; Sheldon *et al.*, 2021). Others have suggested that large variations in seawater pH and certain processes, such as carbonate mineral precipitation and reverse weathering reactions (Equation 1a–e), helped to regulate the global carbon–silica cycle in the Precambrian and thus the input and output fluxes of C and Si between marine sediment sinks, the ocean and the atmosphere (Fig. 2; e.g. Sun & Turchyn, 2014; Isson & Planavsky, 2018; Kasting, 2019; Isson *et al.*, 2020; Krissansen-Totton & Catling, 2020; Torres *et al.*, 2022). All of the mechanisms discussed above are expected to impact atmospheric CO_2 concentrations and climate stability (e.g. Royer *et al.*, 2004).

CO_2 fluxes related to silicate weathering

Five main mechanisms control clay mineral-related fluxes of CO_2 to the atmosphere, which are described in detail by Warr (2022). These are: (1) silicate weathering on the continents, which creates clay mineral covers and crusts that can slow down the rate of rock alteration; (2) organic–clay mineral complexation, which helps to pass dissolved carbon species into the oceans; (3) clay mineral-based pH buffering, which aids carbonate precipitation in the

oceanic environment; (4) reverse weathering reactions, causing clay mineral precipitation onto the seafloor; and (5) crustal diagenesis, metamorphism, melting and volcanism in the upper lithosphere, where (4) and (5) release water and other volatiles (e.g. CO_2) from transforming clay minerals (Fig. 3).
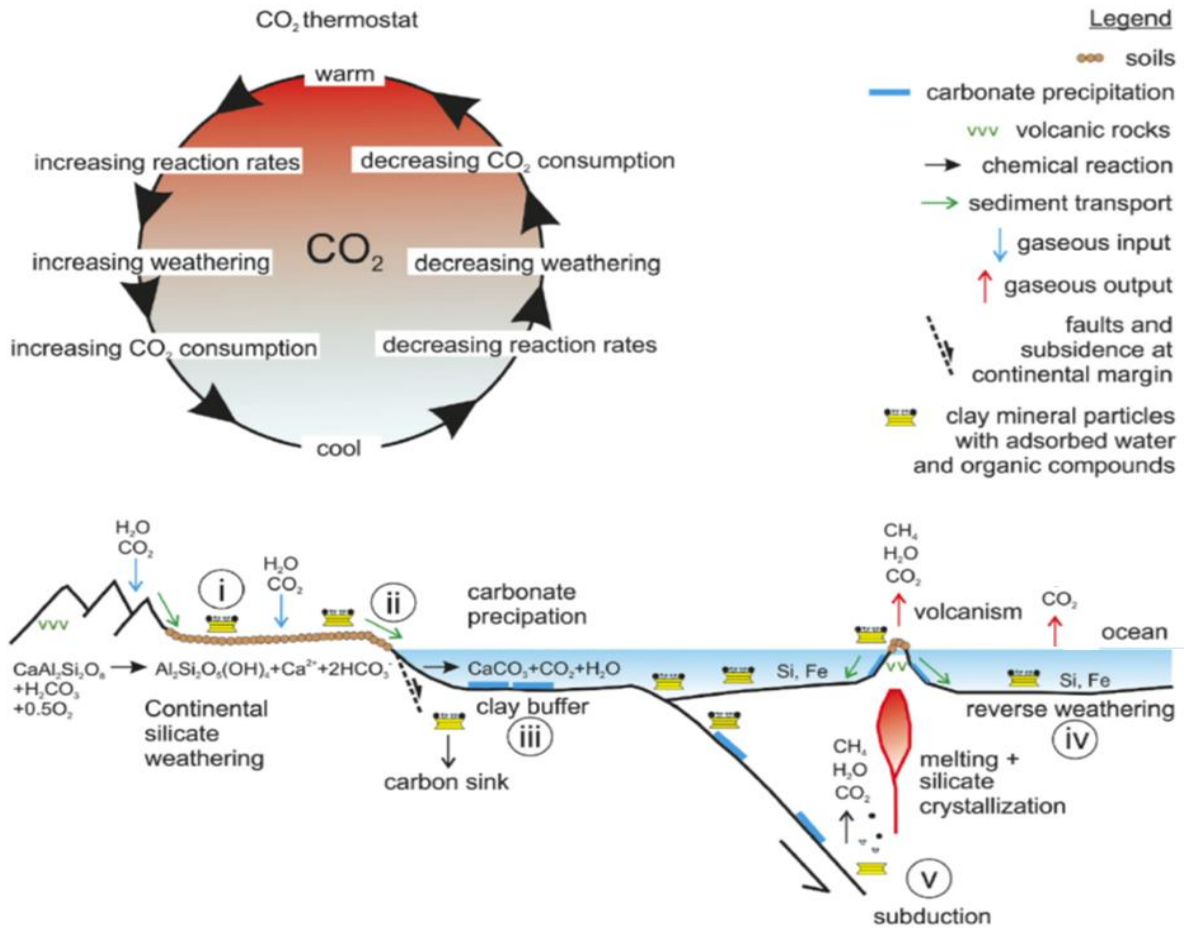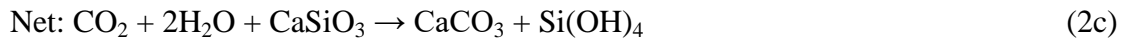

Figure 3. Illustration of the interaction of clay minerals, silicate weathering and atmospheric CO_2 levels. (1) Formation of continental surface clay mineral deposits and weathered crusts consumes CO_2 and slows down rock alteration; (2) organic–clay minerals complexation fixes carbon and passes it into the oceans; (3) clay mineral buffers aid carbonate mineral precipitation in the marine environment; (4) reverse weathering and clay mineral precipitation occur on the seafloor, releasing CO_2; and (5) the release of water and volatiles from clay minerals during subduction enhances crustal melting and volcanism (Warr, 2022, with minor modifications).

Within this context, Earth's climate today is controlled mainly by the (im)balance between CO_2 emissions to the atmosphere and carbon burial by silicate weathering and carbonate formation (e.g. Friedlingstein *et al.*, 2010; Colbourn *et al.*, 2015; Coogan & Gillis, 2020). Carbon removal by marine biogenic and diagenetic–abiogenic carbonate mineral formation consumes the majority of the atmospheric CO_2 inventory (e.g. Torres *et al.*, 2022), as well as some of the ocean-bound carbonate alkalinity sourced from silicate and carbonate weathering on the continents and the deep ocean floor (e.g. Walker *et al.*, 1981; Colbourn *et al.*, 2015). It is believed that the long-term carbon cycle and thus Earth's climate are stabilized by a negative-feedback mechanism known as the silicate weathering thermostat (e.g. Berner *et al.*, 1983; Brantley *et al.*, 2023), which involves temperature- or climate-sensitive atmospheric CO_2 consumption *via* the chemical weathering of susceptible silicate minerals (Figs 2 & 3; e.g. Walker *et al.*, 1981; Kasting, 2019; Jin *et al.*, 2023).

In this widely accepted negative-feedback climate model, silicate weathering is enhanced when pCO_2 and temperature increase, leading to increased consumption of atmospheric CO_2 and hence a cooling effect. As pCO_2 falls, the silicate weathering rate decreases, permitting the build-up of atmospheric CO_2 and consequent warming (e.g. Isson & Planavsky, 2018; Kasting, 2019; Penman *et al.*, 2020). The timescale of the climate response related to changes in silicate weathering is considered to lie in the range of 170–380 kyr, with an average response time of ~240 kyr (Colbourn *et al.*, 2015). As a direct consequence of the described negative-feedback loop, continental and seafloor weathering of primary igneous silicate minerals, such as pyroxene, olivine, amphibole, feldspar and phyllosilicates, is currently considered as a key reaction step for regulating Earth's climate and seawater composition (e.g. Coogan & Gillis, 2013, 2018). As an example, this can be represented by the reactions

show in Equation 2a–c using wollastonite ($CaSiO_3$; e.g. Walker *et al.*, 1981; Berner *et al.*, 1983; Schott *et al.*, 2012; Farkaš *et al.*, 2025):

$$2CO_2 + 3H_2O + CaSiO_3 \rightarrow Ca^{2+} + 2HCO_3^- + Si(OH)_4 \quad\quad\quad (2a)$$

$$Ca^{2+} + 2HCO_3^- \rightarrow CaCO_3 + CO_2 + H_2O \quad\quad\quad (2b)$$

$$\text{Net: } CO_2 + 2H_2O + CaSiO_3 \rightarrow CaCO_3 + Si(OH)_4 \quad\quad\quad (2c)$$
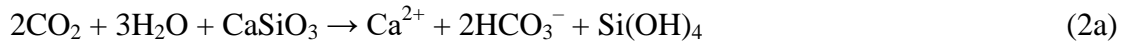
These reactions illustrate how released bivalent cations (mainly Ca^{2+}, but also Ba^{2+}, Mg^{2+}, Mn^{2+}, Fe^{2+}, Sr^{2+} and Zn^{2+}) and carbonate alkalinity are finally deposited as $CaCO_3$ minerals in marine sediments, causing a net reduction of 1 mol of atmospheric CO_2 per 1 mol of $CaCO_3$ formed. In addition, dissolved cations (including also Al^{3+}, Na^+, K^+ and Li^+, among others) and $Si(OH)_4$, if transported to the ocean, can trigger the formation of biogenic opal and authigenic clay minerals in various shallow and deep marine settings (Fig. 1; e.g. Michalopoulos & Aller, 1995; Isson & Planavsky, 2018; Baldermann *et al.*, 2022). However, we note here that clay mineral formation also occurs in various continental settings, such as in soils and lakes (e.g. Huggett & Cuadros, 2010; Bristow *et al.*, 2012; Pozo & Calvo, 2018), although none of these depositional environments belong (by definition) to clay minerals formed through reverse weathering reactions. In any case, the rates of silicate weathering, CO_2 uptake and carbonate mineral precipitation are temperature dependent and therefore can be viewed as representing a planetary thermostat or climate regulator. This is indicated, for example, by the climate-sensitive weathering rates of north-eastern Iceland river catchments (e.g. Gislason *et al.*, 2009) or the terrestrial climate archive from the Valley of Lakes (Mongolia, Central Asia; see Fig. 4; e.g. Baldermann *et al.*, 2021). There, variations in temperature and climatic conditions during the Cenozoic were directly related to pulses of intensified physical *versus* chemical weathering, as is evident by the correlation between the Chemical Index of Alteration (CIA) and excursions of oxygen isotopes ($\delta^{18}O$) recorded in

pedogenic carbonates (e.g. Richoz *et al.*, 2017). The Valley of Lakes continental archive thus provides a sensitive record of changing hydroclimatic conditions, as calcrete (i.e. authigenic calcite) deposited in palaeosols resulted in systematically lighter $\delta^{18}O$ values during wetter conditions and relatively heavier $\delta^{18}O$ values during incursions of drier conditions. Analogously, increased chemical weathering indices (here: the CIA) correspond to periods of wetter conditions, and *vice versa* (Baldermann *et al.*, 2021).
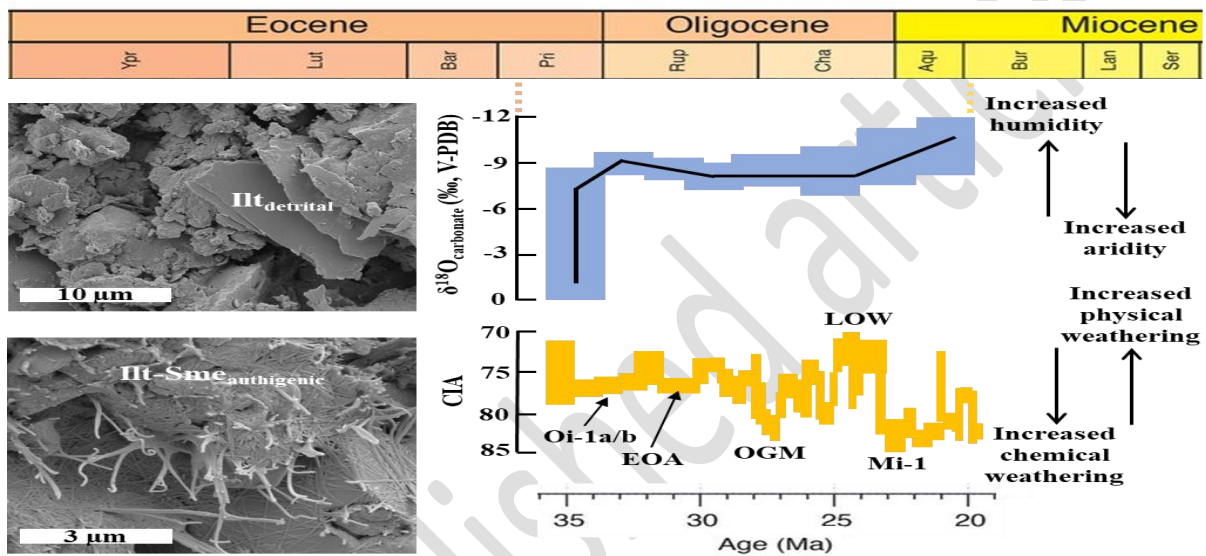
Figure 4. Regional response of pedogenic carbonate oxygen isotope ($\delta^{18}O_{carbonate}$) geochemistry and silicate-based CIA associated with Cenozoic climate change in the Valley of Lakes, Mongolia (source: Baldermann *et al.*, 2021). Note the high sensitivity of the study site to regional and global climatic variability during this time, which is expressed as a higher abundance of detrital illite (Ilt) *versus* authigenic illite-smectite (Ilt-Sme) in periods of increased physical *versus* chemical weathering (see scanning electron miscopy images on the left). Oi-1a/b = Oi-1a/b glaciation (~34–33 Myr); EOA = early Oligocene aridification (~31 Myr); OGM = Oligocene glacial maximum (~28 Myr); LOW = late Oligocene warming (~25 Myr); Mi-1 = Mi-1 glaciation (~23 Myr). Aqu = Aquitanian; Bar = Bartonian; Bur = Burdigalian; Cha = Chattian; Lan = Langhian; Lut = Lutetian; Pri = Priabonian; Rup = Rupelian; Ser = Serravallian; V-PDB = Vienna Peedee Belemnite; Ypr = Ypresian.

The reactivity of Earth's crust (e.g. Gaillardet *et al.*, 1999; Coogan & Dosso, 2015) is also modulated by biological factors, such as the activities of terrestrial plants or soil microbes. As these factors may accelerate or slow down the rates of physical and chemical weathering (e.g. Cuadros, 2017), they are ultimately linked to the regulation of the carbon cycle. These became more important since the advent of biologically active soils and biogenic sediments approximately in the late Neoproterozoic (e.g. Kennedy *et al.*, 2006; Rafiei *et al.*, 2020), as well as the rise of land plants in the Palaeozoic (e.g. Lenton *et al.*, 2012; Porada *et al.*, 2016; McMahon & Davies, 2018; Davies *et al.*, 2020; Isson & Rauzi, 2024). Furthermore, tectonic uplift and topographic elevation (e.g. the Himalayas and the Tibetan Plateau), combined with high precipitation rates, further increased the rate of silicate chemical weathering (and CO_2 consumption) by up to 40–60% (e.g. Raymo & Ruddiman, 1992; Kump & Arthur, 1997; Xu *et al.*, 2024). In addition, the age of an orogen or a mountain belt impacts the rate of silicate weathering. Young orogens weather faster than older ones due to the rapid exhumation of fresh lithologies that are less resistant to chemical weathering processes (e.g. Maher & Chamberlain, 2014).

To summarize, it is widely accepted that changes to global continental weathering have led to fluctuations in atmospheric CO_2 over geological timescales (e.g. Berner, 1990). However, it remains unclear how the combination of tectonic processes, climate change and rock lithologies, among other factors, has influenced the rate of silicate weathering on a global scale (e.g. Hilley & Porder, 2008). Hilley & Porder (2008) calculated a global annual Si weathering flux of 19–46 Tmol, obtained by considering local erosion rates, dust fluxes, temperature and the water balance of various regions worldwide. These authors concluded that the uplift of the Himalayas since the late Cenozoic has had a significant impact on Earth's climate. Similarly, Caves Rugenstein *et al.* (2018) have argued that the Cenozoic

global cooling (~52 Myr to the present day) was mainly triggered by the increasing exposure of highly reactive lithologies exposed in the Himalayas and the Tibetan Plateau. This underlines the importance of the global weathering feedback to Earth's climate evolution, and *vice versa* (Fig. 4; e.g. Caves *et al.*, 2016; Baldermann *et al.*, 2021; Jin *et al.*, 2023). Recently, Lipp *et al.* (2021) have estimated global weathering intensities based on the evolution of the continents' bulk composition over geological time and proposed that silicate weathering was intensified in the Archaean (~25% more CO_2 sequestration between ~4000 and 2500 Myr). This was followed by reduced but relatively constant rates of silicate weathering during the Proterozoic (~2500–541 Myr) and the Phanerozoic (<541 Myr to present). However, these authors also identified peaks in the weathering intensities on shorter timescales within the Phanerozoic, such as during the Carboniferous, Triassic and Cretaceous periods (see fig. 3 in Lipp *et al.*, 2021), illustrating how silicate weathering acts in response to changes in atmospheric CO_2. Similar conclusions were recently drawn by Isson & Rauzi (2024), who have argued that the evolution of Earth's global climate, seawater pH and changes in silicate weathering triggered distinct pulses or declines in early clay mineral diagenesis (i.e. continental and reverse weathering), which are detailed further in later sections of this article.

Early clay mineral diagenesis and climate feedback

Reverse weathering involves the formation of authigenic clay minerals in near-surface marine sediments, a process that consumes carbonate alkalinity and produces acidity and leads to a net release of CO_2 (cf. Equation 1a–e & Fig. 2; e.g. Farkaš *et al.*, 2025). It can proceed *via* entirely *de novo* precipitation of clay minerals, but it can also proceed *via* the partial dissolution of detrital precursor phases, followed by cation enrichment, substitution and restructuring as a 'new phase' (e.g. Garrels, 1965; Mackenzie & Garrels, 1966; Mackin & Aller, 1984). The latter pathway is illustrated by the transformation of kaolinite to berthierine
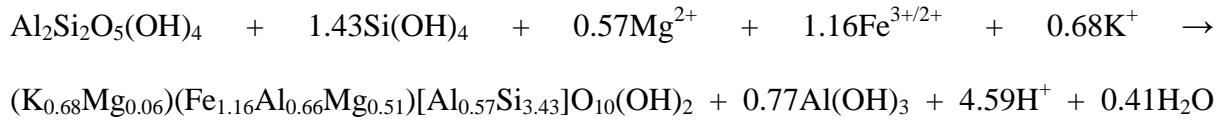
with no additional $Si(OH)_4$ being consumed in this reaction (see Equation 3; Bhattacharyya, 1983):

$$Al_4Si_4O_{10}(OH)_8 + 3Fe^{2+} + 6HCO_3^- \rightarrow Fe_3Al_2Si_4O_{10}(OH)_8 + 2Al(OH)_3 + 6CO_2 \qquad (3)$$
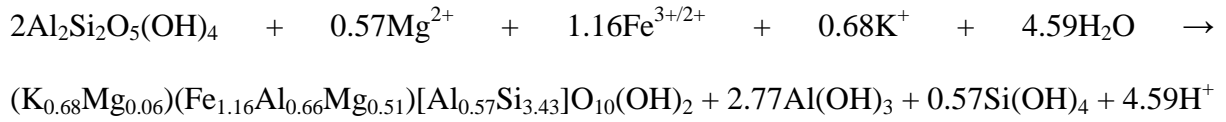
Reverse weathering is thought to have exerted a significant influence on global climate and marine elemental cycling in the past and in the present (e.g. Berner *et al.*, 1983; Mackenzie & Kump, 1995; Baldermann *et al.*, 2022; Isson & Rauzi, 2024), given that the formation of authigenic clay minerals releases CO_2 and impacts on Earth's climate and seawater pH (e.g. Mackenzie & Garrels, 1966b; Kump *et al.*, 2000; Isson & Planavsky, 2018). In simple terms, reverse weathering reactions remobilize carbon species in the ocean–atmosphere system (e.g. Isson & Planavsky, 2018; Farkaš *et al.*, 2025) and act to counterbalance (reverse) the sequestration of carbon linked to silicate weathering (e.g. West *et al.*, 2005). This process can be illustrated *via* the example of kaolinite formation by incongruous weathering of silicates followed by kaolinite alteration to authigenic illite. A standard example of silicate weathering occurring on the continents is the reaction of anorthite ($CaAl_2Si_2O_8$) with dissolved CO_2 (i.e. carbonic acid) at pH 4–6 and at high leaching rates to form kaolinite and alkalinity in (sub)tropical soils (e.g. West *et al.*, 2005; Galán, 2006), according to the reaction in Equation 4:

$$2CO_2 + 3H_2O + CaAl_2Si_2O_8 \rightarrow Ca^{2+} + 2HCO_3^- + Al_2Si_2O_5(OH)_4 \qquad (4)$$

When delivered to marginal marine settings, such as mangrove forests, either 1 or 2 moles of soil-derived, detrital kaolinite (depending on the Si flux) can react further with dissolved cations, provided from saprolite weathering and marine porewater ingress, to form 1 mole of Fe(III)-illite and other components through kaolinite-illitization according to Equation 5a–b (Cuadros *et al.*, 2017):

15

$$Al_2Si_2O_5(OH)_4 + 1.43Si(OH)_4 + 0.57Mg^{2+} + 1.16Fe^{3+/2+} + 0.68K^+ \rightarrow$$

$$(K_{0.68}Mg_{0.06})(Fe_{1.16}Al_{0.66}Mg_{0.51})[Al_{0.57}Si_{3.43}]O_{10}(OH)_2 + 0.77Al(OH)_3 + 4.59H^+ + 0.41H_2O$$

(5a), or

$$2Al_2Si_2O_5(OH)_4 + 0.57Mg^{2+} + 1.16Fe^{3+/2+} + 0.68K^+ + 4.59H_2O \rightarrow$$

$$(K_{0.68}Mg_{0.06})(Fe_{1.16}Al_{0.66}Mg_{0.51})[Al_{0.57}Si_{3.43}]O_{10}(OH)_2 + 2.77Al(OH)_3 + 0.57Si(OH)_4 + 4.59H^+$$

(5b)

It has been proposed that reverse weathering was more efficient under the pervasively silica-rich conditions found in Earth's early oceans, helping to maintain warm, ice-free conditions throughout the Precambrian period (e.g. Isson & Planavsky, 2018). This probably occurred *via* the establishment of a strong relationship between global climate, continental silicate weathering rates, seawater pH and authigenic clay mineral formation, according to the empirical reactions show in Equations 6 & 7:

Silicate weathering: Mafic minerals and glass + CO_2 + H_2O → HCO_3^- + $Si(OH)_4$ + cations (6) Reverse weathering: HCO_3^- + $Si(OH)_4$ + cations → CO_2 + phyllosilicates (7).

Banerjee *et al.* (2016) and Baldermann *et al.* (2022) have also argued that glauconite – the most abundant authigenic clay mineral in the Phanerozoic – preferentially formed during warm climate periods with sea-level high stands, such as in the late Palaeozoic, early Mesozoic and Cenozoic. However, the influence of marine authigenic clay mineral formation on the carbon cycle and seawater pH remains poorly quantified, as the reaction rates are unknown and as the amount of CO_2 released during reverse weathering is probably much lower than the cooling produced by increased silicate weathering reactions that consume CO_2. Further research should assess the kinetics of clay mineral reactions and their influence on the pH sensitivity of aquatic systems, which is required to model the impact of reverse weathering on Earth's CO_2 inventory and climate change (e.g. Isson & Rauzi, 2024).

Carbon cycle models (e.g. Isson & Planavsky, 2018) can incorporate silica (re)cycling and alkalinity consumption through reverse weathering reactions (Equation 1a–e) to account for the formation of berthierine, chamosite, clinochlore, corrensite, glauconite, greenalite, minnesotaite, odinite, saponite, sepiolite and sudoite. These models attempt to provide quantitative estimates on long-term fluctuations in Earth's climate *versus* seawater pH and pCO_2 (e.g. Isson & Planavsky, 2018). It should be noted that the rates of reverse weathering and clay mineral authigenesis in marine sediments are very often considered to be slow (e.g. Ehlert *et al.*, 2016; Baldermann *et al.*, 2018). In contrast, faster reverse weathering rates may occur in proximal and distal marine settings, such as in deltas, estuaries and in some deep-sea environments (e.g. Michalopoulos & Aller, 1995, 2004; Wallmann *et al.*, 2008, 2023; Rahman *et al.*, 2017; Steiner *et al.*, 2022; Geilert *et al.*, 2023). In proximal marine settings, it has been estimated that reverse weathering may sequester 10–50% of the total dissolved silica exported to the modern oceans (e.g. Tréguer & De La Rocha, 2013; Rahman *et al.*, 2016; Tréguer *et al.*, 2021).

The marine silica cycle: biogenic silica *versus* authigenic clay mineral precipitation

Reverse weathering strongly influences the global marine Si cycle *via* the transformation of biogenic and amorphous silica (SiO_2), reactive silicates (e.g. feldspar) or dissolved $Si(OH)_4$ into authigenic clay minerals (e.g. Rahman *et al.*, 2016; Geilert *et al.*, 2023; Wallmann *et al.*, 2023). The individual transformation rates are believed to be relatively slow in open marine settings but may be significantly faster in estuaries, deltas and hydrothermal (deep-sea) environments. Importantly, it is the chemical composition (and temperature) of local marine porewaters that controls the rate of clay mineral authigenesis, with continental margin and shelf settings being particularly favourable. This is probably because the faster and quantitatively more important precipitation of biogenic opal by marine silicifying organisms in the upper water column of the oceans consumes dissolved $Si(OH)_4$, resulting in low

Si(OH)$_4$ concentrations in open, deep marine porewaters, according to the reaction shown in Equation 8:

$$Si(OH)_{4(aq)} \rightarrow SiO_{2(s)} + 2H_2O \tag{8}$$

Throughout the Phanerozoic, the main silicifying organisms have changed, with siliceous sponges expanding in the Cambrian, followed by radiolarians in the Ordovician and diatoms in the Jurassic–Cretaceous (Fig. 5a). Today, such marine biomineralizers account for ~70–90% of the global silica sink (e.g. Tréguer & De La Rocha, 2013; Tréguer *et al.*, 2021). Consequently, modern seawater has a Si(OH)$_4$ concentration (<0.1 mM) that is at least an order of magnitude lower than that inferred for the Precambrian oceans (~1.00–2.21 mM; cf. Fig. 5a; e.g. Siever, 1992; Conley *et al.*, 2017). The modern 'Si-depleted' seawater is therefore unsaturated with respect to the conditions required to precipitate most marine clay minerals (e.g. Baldermann *et al.*, 2018; Isson & Planavsky, 2018), contributing to the reduced number of authigenic clay mineral species forming in the modern ocean compared to the wider array documented in Precambrian marine sedimentary rocks. For example, Han *et al.* (2024) have proposed that widespread evaporitic conditions on the Yangtze Gorges shelf (south China) provided favourable conditions during the Ediacaran for authigenic saponite formation and the development of the Doushantuo Biota.

Isson & Planavsky (2018) have also argued that the rise of silica-biomineralizing eukaryotes may have caused a substantial reduction of the reverse weathering rate in the ancient oceans, resulting in a drop in pCO$_2$ and a change to a less stable climate system by reducing the pH buffer capacity of the global oceans. Such a scenario is consistent with the high diversity of authigenic clay minerals, such as greenalite (Fig. 5b), saponite (Fig. 5c), glauconite and minnesotaite, in the Precambrian geological record, but it is incompatible with the significant increase of glauconite in the marine sediments since the Phanerozoic (Fig. 5a,d). The negative correlation between the Si(OH)$_4$ concentration in Phanerozoic seawater and the

abundance of glauconite in the rock record further suggests that seawater Si was not a limiting factor for this type of marine clay mineral authigenesis. Consequently, the advent of biomineralization and the resulting drop in the seawater Si concentration did not result in the cessation of authigenic clay mineral formation during the Phanerozoic (cf. Equation 8, reverse reaction, & Fig. 5a). Future research should explore the abundance and type of authigenic clay minerals in Precambrian *versus* Phanerozoic marine sedimentary rocks.

Since the emergence and the proliferation of diatoms in the Jurassic–Cretaceous, a drop in the seawater $Si(OH)_4$ concentration occurred (cf. Fig. 5, ~200 Myr; e.g. Conley *et al.*, 2017), which came along with a (time-displaced) increase in the abundance of glauconite in the marine rock record (Fig. 5a). Such a scenario appears to be consistent with the comparatively high abundance of glauconite and celadonite observed in modern coastal and oceanic sediments (e.g. Banerjee *et al.*, 2016; Cuadros *et al.*, 2017; López-Quirós *et al.*, 2019, 2023; Baldermann *et al.*, 2022; Geilert *et al.*, 2023). There, re-mineralization of reactive biogenic opal in the sedimentary pile provides an early diagenetic (secondary) pool of dissolved $Si(OH)_4$, which is required for clay mineral formation (e.g. Vorhies & Gaines, 2009; Isson & Planavsky, 2018; Woltz *et al.*, 2023). This process illustrates the linkage between biogenic opal formation and early diagenetic re-mineralization and clay mineral authigenesis, which is expressed by Equation 9:

$$SiO_{2(s)} + Al(OH)_3 + (Mg^{2+}, Na^+, K^+, Fe^{2+/3+}) + HCO_3^- \rightarrow \text{Authigenic clays} + CO_2 + H_2O \quad (9)$$
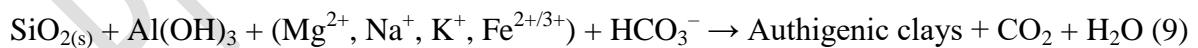
Despite the above relationships, porewater data collected from shelf, slope and deep-sea sites across modern oceans indicate that the dissolved $Si(OH)_4$ concentration is generally too low and not favourable for more extensive marine clay mineral authigenesis (e.g. Isson & Planavsky, 2018). This is mainly due to the high degree of bio-opal remineralization occurring in the upper water column of the oceans (~70%), the regionally uneven distribution of bio-opal production and the rapid vertical diffusion of porewater-related $Si(OH)_4$ to the Si-

depleted bottom seawater. All of these factors prevent the establishment of the high concentrations of $Si(OH)_4$ at the sediment–seawater interface that are required for authigenic clay mineral formation (e.g. Tréguer & De La Rocha, 2013). The notable exceptions are glauconite, nontronite, saponite and sepiolite-palygorskite group clay minerals with the right compositions to form in marine environments. According to hydrochemical modelling of modern seawater and porewater compositions, these require comparatively low amounts of dissolved $Si(OH)_4$ to precipitate (e.g. Baldermann *et al.*, 2018; Isson & Planavsky, 2018). However, it has been frequently documented that authigenic clay minerals can precipitate directly on dissolving biogenic silica particles, which could imply that at least the reactive parts of siliceous skeletons react *in situ* to form phyllosilicates (e.g. Michalopoulos *et al.*, 2000; Presti & Michalopoulos, 2008; Loucaides *et al.*, 2010; Baldermann *et al.*, 2013; López-Quirós *et al.*, 2019; Geilert *et al.*, 2023). This is presumably because the local pore fluid $Si(OH)_4$ concentration at this reactive interface is much higher than that measured in the bulk fluid, generating geochemical microenvironments that favour clay mineral authigenesis, as confirmed by the hydrochemical modelling of modern porewater compositions (e.g. Wallmann *et al.*, 2023).

Consequently, it is the variation of the local dissolved $Si(OH)_4$ concentration in porewaters across geological time that controlled the rate and magnitude of authigenic clay mineral formation. Whereas biogenic opal mineralization may have decreased the average seawater Si concentration, the massive sedimentation of siliceous components may have favoured large local porewater or early diagenetic micromilieu $Si(OH)_4$ concentrations that helped to boost the authigenesis of diverse clay mineral species. In the Precambrian, the global ocean was likely to have been anoxic (Fe-rich) and rich in $Si(OH)_4$ (e.g. Siever, 1992; Poulton & Canfield, 2011; Conley *et al.*, 2017; Tosca *et al.*, 2019), favouring the deposition of, for example, extensive silica-rich banded iron formations (BIFs), as well as greenalite and other

marine clay minerals (e.g. Rasmussen *et al.*, 1998, 2013, 2017, 2021; Klein, 2005; Johnson *et al.*, 2018; Tosca *et al.*, 2019; Muhling & Rasmussen, 2020). The latter Fe-phyllosilicates not only occur in distinct and separate sedimentary units; they also appear as encapsulated pockets and inclusions in early diagenetic chert (Fig. 5b). This implies that authigenic clay minerals, despite their tendency to dissolve, dehydrate and/or transform during diagenesis and metamorphism, could have been more abundant in the Precambrian record than recently thought or preserved in the rock record (e.g. Morris, 1993; Klein, 2005; Rasmussen *et al.*, 2017; Isson & Planavsky, 2018; Huang *et al.*, 2024; Isson & Rauzi, 2024). This abundance of clay minerals formed by reverse weathering would have potentially impacted the global climate at that time.

In contrast, Dunlea *et al.* (2017) suggested that during the Cenozoic (~66 Myr until today) stagnating rates of marine authigenic clay mineral formation (Fig. 5a) caused seawater Mg/Ca to rise and atmospheric CO_2 to decline over the past ~50 Myr. This was linked to the remarkable Cenozoic global cooling that continued until the beginning of the temperature rise in the late Pleistocene. This latter relationship highlights the complex links between the global marine element cycles and Earth's climate response – features that are evident in the diversity of authigenic clay minerals found in the geological record.
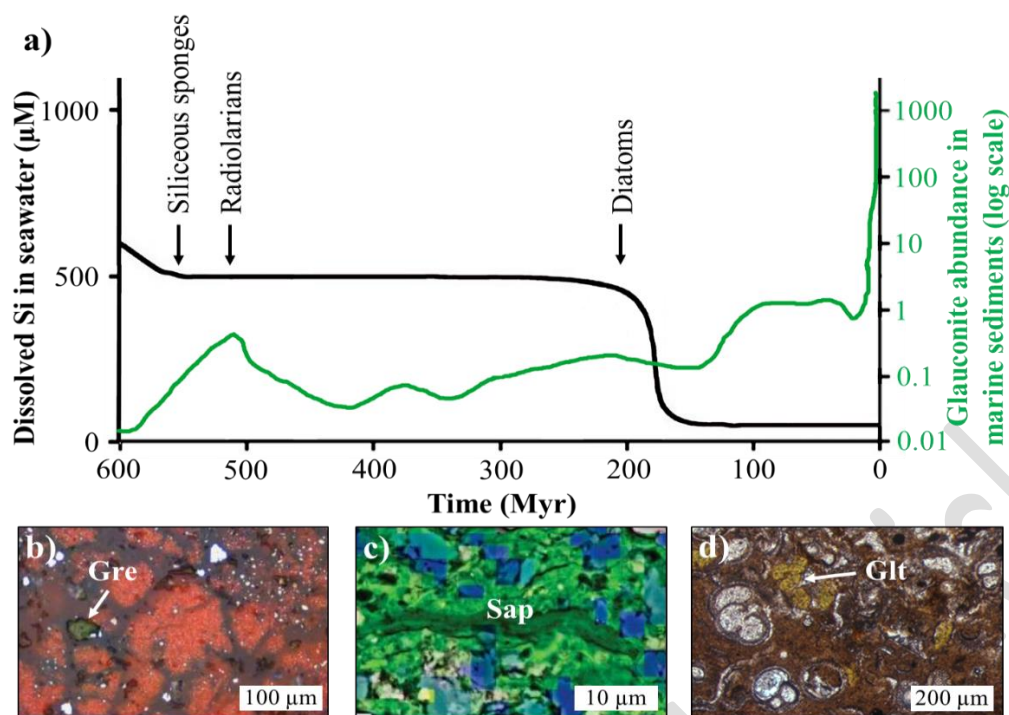
Figure 5. (a) Relationship between the evolution of marine siliceous organisms, the dissolved Si concentration in the ocean (data source: Conley *et al.*, 2017) and the abundance of glauconite in the geological record (data source: Banerjee *et al.*, 2016) from the early Precambrian to the present. The glauconite abundance (in %) is expressed by the logarithm of the actual number of occurrences in different intervals divided by the time duration. The sedimentation and early diagenetic re-mineralization of biogenic opal probably provided porewater $Si(OH)_4$ favouring clay mineral authigenesis. (b) Photomicrograph showing authigenic greenalite (Gre; marked with white arrow) embedded in a greyish chert and reddish hematite matrix from the Late Archean Kushtagi-Hungund Schist Belt (India). (c) Artificially coloured scanning electron microscopy with energy-dispersive X-ray spectroscopy mineral map displaying authigenic saponite (Sap) hosted in a blueish dolomite matrix from the Ediacaran Doushantuo Formation (China). (d) Photomicrograph showing glauconite (Glt; marked with white arrow) growing in foraminiferous ooze in Pleistocene–Holocene-aged Ivory Coast–Ghana Marginal Ridge sediments. Images (b)–(d) are provided by AB.

22

Stratigraphic distribution of authigenic clay minerals in the marine rock record

In this section, an overview is given of the stratigraphic and temporal distributions of authigenic clay minerals that typically form in the marine realm during early diagenesis (cf. Fig. 1). Secondary clay mineral assemblages that may precipitate in the continental critical zone and during late diagenesis are not considered, as these minerals do not represent reverse weathering products. However, we emphasize that recognizing and quantifying the frequently fine-grained products of reverse weathering reactions in the marine rock record are challenging (e.g. Hazen *et al.*, 2013; Han *et al.*, 2022a), given that authigenic clay minerals are commonly intermingled with clay minerals of detrital origin or have been partly overprinted by deep burial diagenetic reactions. Therefore, marine clay minerals are typically of diverse origin. However, most of the truly authigenic clay minerals found in marine sediment archives are Fe-rich (here: 12 out of the 18 clay minerals considered; Hazen *et al.*, 2013). The reasons for the dominance of authigenic clay minerals enriched in Fe(III) and/or Fe(II) over Fe-poor or Fe-depleted clay minerals in marine sediments remain disputed, but controlling factors may include the early diagenetic Fe(III) reduction coupled to complex inorganic and biological processes and the progressive decay of organic matter. These reactions provide (partly organo-complexed) reactive Fe^{2+} and also Fe^{3+} ions to the marine porewater inventory, from which authigenic Fe-rich clay minerals tend to precipitate (see earlier).

Beidellite and chlorite-smectite

Beidellite is a rather uncommon mineral of the dioctahedral smectite group that has been documented mainly in Cretaceous sequences (Figs 6 & 7). It is thought to have formed by the alteration of montmorillonite in the presence of dissolved $Fe^{3+/2+}$, typically under the elevated

temperatures of mid-oceanic ridge sites (e.g. Post *et al.*, 1997; Bouna *et al.*, 2012). Orange-coloured beidellite has been found in macropores and intergranular pores of altered mafic host rocks, together with intergrowths of zeolites, goethite and greenish-brown chlorite-smectite mixed-layered clay minerals (e.g. Hu *et al.*, 2023). Corrensite, an ordered chlorite-smectite group mineral, is locally found in hydrothermally altered marine clastic sediments and ophiolitic rocks. For example, Buatier *et al.* (1995) reported that authigenic corrensite formed ~32 m below the sediment–seawater interface at 300°C ± 30°C during active hydrothermal venting at the axial rift valley of the northern Juan de Fuca Ridge.

Berthierine

Berthierine, the Fe member of the serpentine mineral group, formed preferentially as oolitic grain infills (together with chamosite) during Palaeozoic and Mesozoic times (Figs 6 & 7). In the Jurassic and Cretaceous, it formed by the alteration of volcanogenic particles in oxygen-depleted seawater (e.g. Maynard, 1986; Rudmin *et al.*, 2022a; Kalinina *et al.*, 2024; Roy Choudhury *et al.*, 2024). Reactions involved the transformation of siderite, kaolinite, odinite, chamosite and glauconite precursor grains under reducing conditions (e.g. Iijima & Matsumoto, 1982; Bhattacharyya, 1983; Hornibrook & Longstaffe, 1996; Tang *et al.*, 2017) or the alteration of transported laterite-derived materials under reducing, marine porewater conditions (e.g. Fritz & Toth, 1997; Toth & Fritz, 1997). The availability of dissolved Fe^{2+} is key to the formation of yellowish-greenish-brownish berthierine in shallow marine, estuarine and fresh to brackish settings under (sub)tropical conditions (Fig. 8a). In some cases, berthierine has been documented in near-coastal coal-forming environments (Iijima & Matsumoto, 1982) and marine hydrothermal surroundings (Taylor, 1990; Roy Choudhury *et al.*, 2024).

Celadonite

This mineral of the Fe- and K-rich mica group preferentially forms as vesicle fillings and as massive aggregates in altered basaltic rocks (Fig. 8b). It is common in the Proterozoic, often in association with BIFs (e.g. Savko, 2006), but it is most abundant in the well-preserved Mesozoic rock record (Figs 6 & 7), probably because of the peak mid-oceanic ridge length and fast seafloor spreading rates at that time (e.g. Müller *et al.*, 2013, 2022). The most favourable conditions for the formation of bluish-green celadonite developed in the Cretaceous, when this mineral was primarily formed by the *in situ* alteration of mafic and intermediate volcanic rocks in the presence of either marine or meteoric fluids rich in K^+, $Fe^{3+/2+}$ and Mg^{2+} ions (e.g. Baker *et al.*, 2012). Even though celadonite and glauconite can precipitate under similar physicochemical conditions, celadonite is rarely found in Palaeozoic successions and modern oceanic sediments and volcanic rocks (e.g. Singh *et al.*, 2023).

Chamosite

Even though chamosite, the Fe^{2+} member of the chlorite group, has formed in marine sediments since the Precambrian, the best conditions for its crystallization prevailed during the Ordovician, Silurian, Devonian and Jurassic to Neogene (Figs 6, 7 & 8c). Favourable conditions for the precipitation of authigenic chamosite often occurred in close association with the formation of ooidal ironstones, where the supply of dissolved Fe^{2+} and Mg^{2+} ions from detrital sources or reducing marine fluids and the leaching of $Si(OH)_4$ and K^+ ions from reactive precursor clays, such as berthierine or glauconite, triggered the formation of this mineral (e.g. Mücke, 2006; Tang *et al.*, 2017). However, the burial diagenetic or hydrothermal formation of chamosite from smectite is also possible. The stratigraphic distribution and the abundance of authigenic chamosite, a relatively common marine clay mineral, which often appears with a greyish-greenish-brown colour, commonly overlap to some degree with those of glauconite (e.g. Van Houten & Bhattacharyya, 1982; Rudmin *et*

25

al., 2019, 2021). Chamosite has, however, also been reported in Proterozoic sequences, where Fe^{2+}- and $Si(OH)_4$-rich seawater facilitated its formation by ion exchange between the sediment, porewater and seawater (e.g. Tang *et al.*, 2017).

Glauconite

This Fe-rich mica group mineral was commonly precipitated as light to dark green rounded concretions (pellets) during the Precambrian, Mesozoic and Cenozoic (Figs 6 & 7). The Late Cretaceous and Palaeogene marked notable periods of glauconite formation on the continental shelves of that time. Factors that facilitated the formation of glauconite (and of its precursor, Fe(III)-smectite) during greenhouse climates included the availability of dissolved $Si(OH)_4$, $Fe^{2+/3+}$, K^+ and Mg^{2+} in seawater or sediment porewater, the presence of microenvironments, such as faecal pellets, bioclasts and corroded feldspar, and the development of oxygen-depleted conditions at the sediment–seawater interface (e.g. Odin, 1988; Meunier & El Albani, 2007; Charpentier *et al.*, 2011; Baldermann *et al.*, 2012; Gaudin *et al.*, 2015; Banerjee *et al.*, 2016; Zhang *et al.*, 2022b). Glauconite formation was also favoured by global sea-level fluctuations and low sedimentation rates (e.g. Roy Choudhury *et al.*, 2022). The early diagenetic precipitation of glauconite and other ferric illites contributed significantly to the marine sinks of Fe, Mg, K, Si and Al (e.g. Cuadros *et al.*, 2017; Baldermann *et al.*, 2022). In contrast, during the Holocene the authigenic glauconite grains formed almost exclusively in deep marine sediments (Fig. 8d).
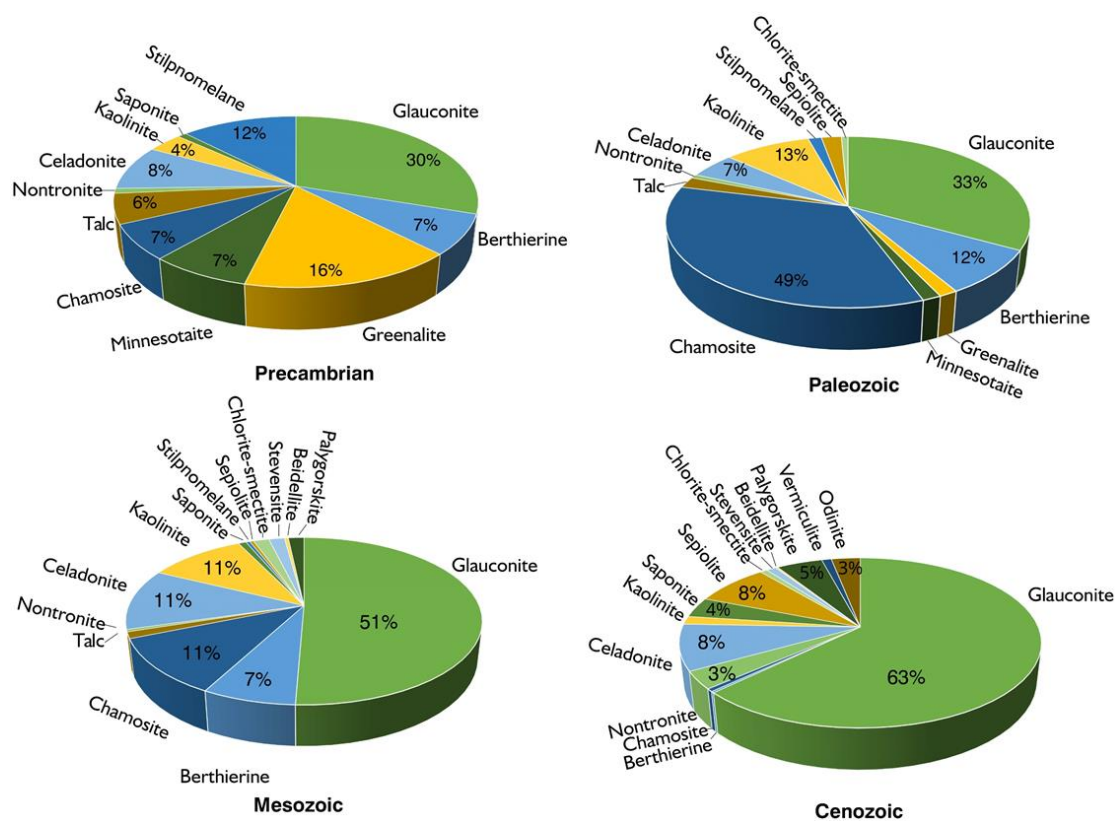
Figure 6. Temporal distribution of authigenic clay minerals found in different sedimentary environments across geological time. The occurrence of authigenic clay minerals is provided in Table S1; however, the nature of kaolinite is disputed – it can be of detrital or authigenic origin. Note that glauconite is the most abundant authigenic clay mineral across time, whereas chamosite is particularly abundant in the Palaeozoic.

Greenalite

This uncommon Fe-rich mineral of the serpentine group primarily formed in the Precambrian in close association with BIF deposits (Figs 6, 7 & 8e). Some appearances have also been documented in the Palaeozoic and Mesozoic rock records (e.g. Rasmussen *et al.*, 1998, 2021; Grenne & Slack, 2019; Ghosh, 2020). Greenalite formation from amorphous Si- and Fe-bearing precursor phases in the Archaean ocean (e.g. Tosca *et al.*, 2016, 2019; Rasmussen *et al.*, 2017, 2021) was likely favoured by the enrichment of Fe^{2+}, as well as Al^{3+}, Mg^{2+} and

27

Si(OH)$_4$ in near-surface sediments (e.g. Johnson *et al.*, 2018; Mohanty & Mishra, 2023). Hydrothermal sources have been suggested to have contributed to the source of Fe in greenalites (e.g. Tosca *et al.*, 2019; Muhling & Rasmussen, 2020; Tosca & Tutolo, 2023; Tostevin & Ahmed, 2023).
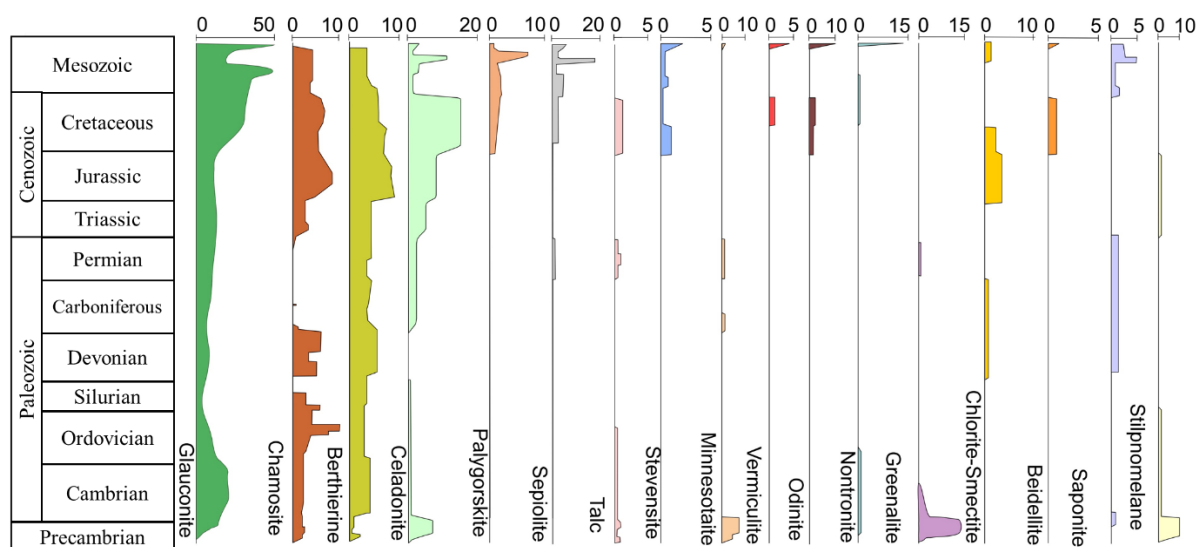
Figure 7. Stratigraphic distribution of common clay minerals found in various sedimentary environments. Kaolinite is not shown because the great majority of kaolinite occurrences are considered to be of detrital rather than marine authigenic origin. The numbers at the top represent the numbers of published occurrences of specific authigenic clay minerals provided in Table S1.

Kaolinite

Kaolinite, the dioctahedral member of the kaolinite-serpentine group, occurs as a chemical weathering product in all rock types (e.g. Stoch & Sikora, 1976). Its formation and enrichment in soils and shelf sediments were favoured during the Jurassic and Cretaceous (Fig. 7). Although most of the kaolinite found in continental shelf and deep-sea sediments is

28

detrital in origin, some occurrences have been attributed to reverse weathering (e.g. Maliva *et al.*, 1999; Pe-Piper *et al.*, 2005). Hydrothermal alteration also induces kaolinization by the removal of $Si(OH)_4$, K^+, Mg^{2+} and $Fe^{2+/3+}$ from volcanic glasses and mafic minerals in both terrestrial and marine environments (e.g. Altschuler *et al.*, 1963; Erkoyun & Kadir, 2011; Kadir *et al.*, 2011).

Minnesotaite

This Fe-silicate mineral belonging to the pyrophyllite-talc group mainly formed in the Precambrian, but minor occurrences have also been documented in Lower Carboniferous and Permian sequences (Figs 6 & 7). Minnesotaite deposits are often associated with BIFs, where greenish-grey to olive-green aggregates of fine needles and platelets probably formed *via* the alteration of greenalite under reducing conditions and in the presence of fluids with a high Mg/Fe ratio (e.g. Blake, 1965; Rasmussen *et al.*, 1998; Lempart-Drozd *et al.*, 2022).

Nontronite

This yellowish-green (brownish-orange when weathered) Fe^{3+} member of the smectite group formed dominantly in the Precambrian, Cambrian, Cretaceous, Palaeogene and Neogene as an alteration product of mafic minerals at mid-oceanic ridge sites or in close association with ironstone deposits, as well as in continental soils (e.g. Köhler *et al.*, 1994; Dekov *et al.*, 2007; Afify *et al.*, 2015, 2018; Rudmin *et al.*, 2022b). However, nontronite (or Fe(III)-smectite in general) may also precipitate in (semi)confined marine microenvironments at low temperatures and subsequently act as a precursor phase to glauconite formation (e.g. Baldermann *et al.*, 2013).

Odinite

Odinite is a rare, Fe(III)-enriched clay mineral of the kaolinite group. It formed in ancient and modern shallow marine settings, lagoons, pro-deltas and estuaries characterized by warm

waters enriched in dissolved Fe^{3+}, Mg^{2+} and $Si(OH)_4$, such as in the Cretaceous (Figs 6 & 7; e.g. Bailey, 1988). Due to its high reactivity, odinite rapidly alters to berthierine and chlorite (e.g. Hornibrook & Longstaffe, 1996; Šegvić *et al.*, 2020).

Palygorskite

Palygorskite is a relatively uncommon mineral in the marine rock record. It formed either by the transformation of sepiolite, smectite and volcanic ash or as a precipitate from pore fluids rich in $Si(OH)_4$ and Al^{3+} and Mg^{2+} ions (e.g. Yalçin & Bozkaya, 2011), preferentially in the Cretaceous and Neogene (Figs 6 & 7; e.g. Akbulut & Kadir, 2003; Galán & Pozo, 2011). Microstructural and mineralogical evidence suggests that the purest palygorskite deposits of Cretaceous to Palaeogene age were formed *in situ* by reverse weathering on the seafloor (e.g. Thiry & Pletsch, 2011). Palygorskite forms a complete solid solution with sepiolite and primarily occurs in lacustrine, fluvial, (peri)marine and soil environments (e.g. Isphording, 1973; Galán & Pozo, 2011).

Saponite

The trioctahedral (Mg-rich) smectite group mineral saponite mainly formed during the Cenozoic, although rare occurrences of this mineral have been reported in the Precambrian, Devonian and Permian (Figs 6 & 7). Precambrian saponite preferentially formed in restricted, evaporitic lagoons that were temporally connected to the ocean (e.g. Han *et al.*, 2022b). Bluish-green (reddish-brown when weathered) saponite is also known to form *via* the alteration of mafic rocks or volcanic matter under the influence of hydrothermal fluids in marine settings (Fig. 8f), as well as in evaporitic and alkaline lakes (e.g. Andrews, 1980; Post, 1984; Akbulut & Kadir, 2003; Rudmin *et al.*, 2023a).
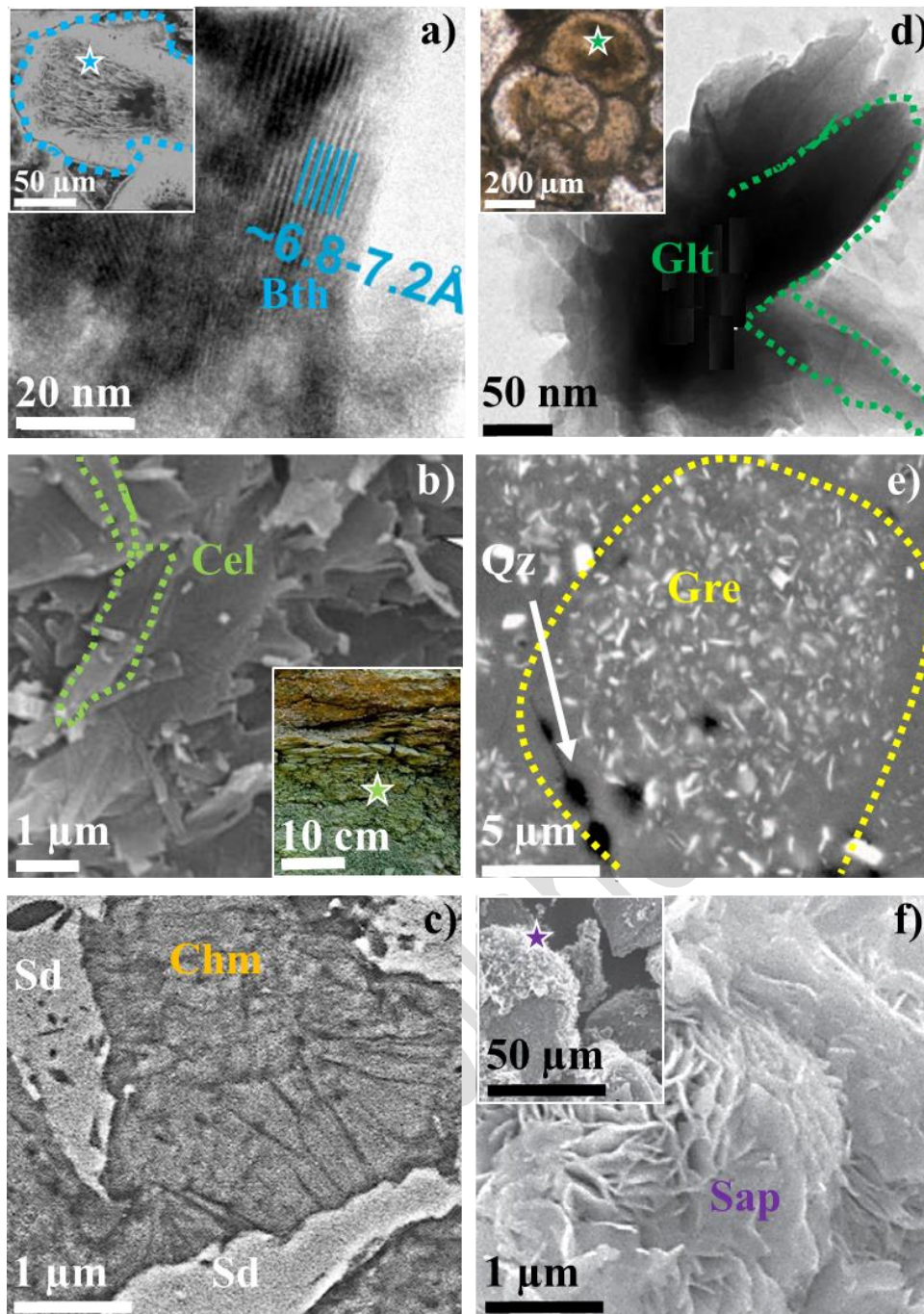
Figure 8. Transmission electron microscopy and scanning electron microscopy images of common authigenic clay minerals formed during reverse weathering across geological time. (a) Fibrous berthierine (Bth) crystals (~7 Å) infilling ooids (inset image) from the Oligocene channel ironstones of the Lisakovsk deposit in Kazakhstan (Rudmin *et al.*, 2021). (b) Lath-like celadonite (Cel) particles occurring in interstitial and void spaces in green bole beds (inset image) within the Late Cretaceous Deccan Volcanic Province in India. This Cel formed

in a non-marine environment, but it otherwise precipitated under submarine conditions (Singh *et al.*, 2022). (c) Microcrystalline chamosite (Chm) and siderite (Sd) spar from the Middle Triassic Kremikovtsi Sedimentary Exhalative Siderite Iron Formation in Bulgaria (Damyanov & Vassileva, 2001). (d) Lath-like glauconite (Glt) infilling foraminifera tests (inset image) at the Ivory Coast basin close to the Ghana continental margin (Baldermann *et al.*, 2013). (e) Fibrous greenalite (Gre) crystals in polygon-shaped quartz (Qz) grains from the Proterozoic-aged Brockman Iron Formation in Australia (Rasmussen *et al.*, 2021). (f) Honeycomb-like saponite (Sap) aggregates covering the surface of altered basalt grains (Voigt *et al.*, 2020). Coloured stars in the low-resolution images indicate the positions of regions of interest used for high-resolution imaging.

Sepiolite

This hydrous Mg-rich silicate mineral is found in abundance in Cenozoic marine sediments (together with palygorskite), but minor occurrences have also been reported from Permian and Cretaceous strata (Figs 6 & 7). Fluids rich in Mg^{2+} and $Si(OH)_4$ facilitated the formation of sepiolite in (peri)marine, transitional and lacustrine environments (e.g. Akbulut & Kadir, 2003; Yalçin & Bozkaya, 2011; Sánchez-Roa *et al.*, 2016). Sepiolite may also form *via* the hydrothermal alteration of basalts and volcanic ash (e.g. Akbulut & Kadir, 2003; Galán & Pozo, 2011; Pozo & Calvo, 2018).

Stevensite

Stevensite is a trioctahedral (Mg-rich) smectite group mineral that often formed by precipitation in alkaline and playa lakes (e.g. de Oliveira Nardi Leite *et al.*, 2020; Netto *et al.*, 2022). This mineral mainly formed from the Cretaceous to recent (Figs 6 & 7) within ooids, peloids and intraclasts in Mg^{2+}- and $Si(OH)_4$-rich lacustrine and coastal marine settings, and

more rarely by the alteration of oceanic crust under the influence of hydrothermal fluids (e.g. Banfield *et al.*, 1991; Cuevas *et al.*, 2003; Armelenti *et al.*, 2016; Lima & De Ros, 2019).

Stilpnomelane

This blackish-greenish-yellowish smectite group mineral formed mainly during the Precambrian and Mesozoic (Figs 6 & 7) within marine Fe-rich deposits, such as BIFs, that received upwelling of Fe^{2+}- and $Si(OH)_4$-rich deep-seated (hydrothermal) fluids mixed with shallower and slightly oxygenated seawater (e.g. Garzanti *et al.*, 1989; Pickard, 2003; Wang *et al.*, 2015).

Talc

This Mg member of the talc-pyrophyllite group is a relatively rare authigenic mineral in the sedimentary rock record. It mostly formed in Precambrian, Permian and Cretaceous strata (Figs 6 & 7) under the influence of Al-poor and $Si(OH)_4$- and Mg-rich fluids under marine (or lacustrine) conditions (e.g. Noack *et al.*, 1989; Chen *et al.*, 2002; Tosca *et al.*, 2011; Han *et al.*, 2024). Rarely, talc also formed by the alteration of sepiolite under the influence of microbial activity and in the presence of $Si(OH)_4$-rich marine pore fluids.

Vermiculite

Dioctahedral vermiculite, an expandable and abundant clay mineral in continental soils, typically formed by the chemical weathering or the alteration of amphibole, biotite and phlogopite precursors (e.g. Wilson, 2004). However, vermiculite is a rather uncommon mineral in the marine rock record, with some rare occurrences being documented in the Cretaceous and Pleistocene to recent times (Figs 6 & 7). In these rocks, vermiculite appears in its trioctahedral form, typically within interstratified illite-vermiculite and chlorite-vermiculite (e.g. Craw *et al.*, 1995; Gutierrez-Mas *et al.*, 1997; Yin *et al.*, 2018).

Reverse weathering and clay mineral authigenesis across geological time

Earth's greenhouse climatic periods clearly influenced the rates of reverse weathering and the associated distribution and abundance of authigenic clay minerals in marine sediments across geological time. Such periods were characterized by an elevated seawater temperature (on the shelf), a higher continental (dissolved) element export to the oceans, comparatively higher $Si(OH)_4$ concentrations in marine porewaters and enhanced microbial activity that catalysed reverse weathering reactions (e.g. Schieber *et al.*, 2007; Aubineau *et al.*, 2019, 2020). In this section, some examples are provided of specific periods that favoured clay mineral authigenesis in the oceans and along the submerged continental margins.

Precambrian palaeoclimate

The authigenesis of a suite of Fe(II/III)-phyllosilicates (cf. Fig. 7) in the Precambrian ocean is believed to have released significant amounts of CO_2, which helped maintain the warm and ice-free global climate despite the much lower solar luminosity at that time (e.g. Isson & Planavsky, 2018; Han *et al.*, 2024). Glauconite formed dominantly on marine shelves during the Late to Middle Proterozoic, resulting in thick glauconitic sandstones and glauconitic mudrock deposits in many places worldwide (e.g. Banerjee *et al.*, 2008, 2016; Mandal *et al.*, 2020, 2022). The formation of sedimentary greenalite in the Palaeoproterozoic and of authigenic talc in the Neoproterozoic was facilitated by high Fe^{2+}, Al^{3+}, $Si(OH)_4$ and Mg^{2+} concentrations in seawater (e.g. Tosca *et al.*, 2011, 2016; Mohanty & Mishra, 2023; Tostevin & Ahmed, 2023). Moreover, authigenic saponite formed in restricted evaporitic lagoons over large areas of the Yangtze Gorges shelf in south China from Mg^{2+}- and $Si(OH)_4$-rich Ediacaran seawater (e.g. Han *et al.*, 2022b, 2024). A combination of palaeo-environmental factors, such as the widespread presence of suboxic seawater masses, the absence of marine silicifying organisms, adequate seawater chemistry and the overall low sedimentation rates (e.g. Eriksson *et al.*, 2001; Banerjee *et al.*, 2008), favoured the authigenesis of Fe-silicates in the Precambrian (e.g. Banerjee *et al.*, 2008; Mandal *et al.*, 2020). Reverse weathering was

also facilitated by microbial activity, as is evident from the Precambrian-aged microbial mat deposits enriched in Fe-illite, ferroan illite-smectite, stilpnomelane and minnesotaite (e.g. Konhauser & Urrutia, 1999; Schieber *et al.*, 2007; Rasmussen *et al.*, 2013; Konhauser *et al.*, 2017; Aubineau *et al.*, 2020). These microbial biofilms trapped K^+ ions from the seawater and released them into the porewater during the degradation of organic matter at early diagenesis, but they also provided the porewater with other important ions, such as $Fe^{2+/3+}$, during respiration. This resulted in the progressive illitization of smectite precursors, as well as in the neoformation of K- and Fe-phyllosilicates, which subsequently acted as mineral archives that allow us to identify biomineralization processes on ancient Earth (e.g. Vorhies & Gaines, 2009; Aubineau *et al.*, 2019).

Late Palaeozoic to early Mesozoic warming

The Ordovician to Devonian timespan, as well as the Jurassic, witnessed the formation of authigenic chamosite and berthierine in massive ooidal ironstone facies (cf. Fig. 7). Mid-Ordovician-aged chamositic ironstones formed on storm-dominated shelves characterized by Fe^{2+}-rich sea-bottom conditions (e.g. Dunn *et al.*, 2021). The authigenesis of these Fe(II)-rich clay minerals that occurred during such periods was linked to a sea-level highstand, the presence of oxygen-depleted but cation-rich seawater, microbial mediation and a warm climate (e.g. Van Houten & Arthur, 1989; Young, 1989; Li *et al.*, 2021b).

Mesozoic greenhouse

Glauconite authigenesis was significant during transgressive events in the Cretaceous (cf. Fig. 7), especially from the Aptian to the Maastrichtian (e.g. Bansal *et al.*, 2020, 2021). The higher temperature and suboxic seawater enriched in K^+, Mg^{2+}, $Si(OH)_4$ and Fe^{2+} ions, coupled with a sea-level highstand during the Cenomanian greenhouse conditions, facilitated the high abundance of glauconite on the marine shelves (e.g. Haq, 2014; Banerjee *et al.*,

2016; Baioumy *et al.*, 2020; Wilmsen & Bansal, 2021; Scheiblhofer *et al.*, 2022). The formation of glauconite probably sequestered significant amounts of K, Fe, Mg, Si and Al from Cretaceous seawater (e.g. Baldermann *et al.*, 2022). Upper Cretaceous glauconite deposits mainly formed along the margins of the Tethys Ocean (e.g. Bansal *et al.*, 2020). In addition, a high abundance of other authigenic clay minerals has been documented for the Cretaceous, such as berthierine, celadonite, palygorskite, talc, stevensite and beidellite (cf. Fig. 7), which was possibly related to a fast sea-level rise, warm seawater and high seafloor spreading rates at mid-oceanic ridges at that time (e.g. Jeans, 2006; Müller *et al.*, 2013, 2022; Singh *et al.*, 2023). In addition, chamositic-siderite ironstone deposits formed during Oceanic Anoxic Event 3, and abundant Jurassic chamositic-ooidal ironstones precipitated at the Neo-Tethyan margin due to upwelling and fluctuating redox conditions against the backdrop of Mesozoic greenhouse conditions (e.g. Van Houten & Arthur, 1989; Han *et al.*, 2023).

Cenozoic greenhouse climate

The Cenozoic era was marked by several hyperthermal events, which were associated with abundant authigenic Fe(II/III)-phyllosilicates preserved in the marine sedimentary record (cf. Fig. 7). Glauconitization was frequent due to a high sea level and warm greenhouse conditions since at least the Cretaceous (e.g. Baldermann *et al.*, 2022), with maximum occurrences documented during hyperthermal events in the Palaeogene, Eocene and Oligocene (e.g. Banerjee *et al.*, 2020). A multi-proxy study by Roy Choudhury *et al.* (2022), which applied biostratigraphy, carbon isotopes, Sr concentrations and ^{40}Ar/^{39}Ar chronostratigraphic data, demarcated the Palaeogene hyperthermal events as being remarkably rich in glauconite deposits, such as those reported for the Palaeocene–Eocene Thermal Maximum. The combination of oceanic hypoxia, warm climate conditions and rapid sea-level changes during the Palaeogene temperature maxima favoured the formation of glauconite deposits (e.g. Banerjee *et al.*, 2020; Roy Choudhury *et al.*, 2022). Before that time,

around the Cretaceous–Paleogene boundary, ooidal ironstones were deposited, which contain abundant chamosite, berthierine and glauconite (e.g. Rudmin *et al.*, 2017).

Modern-day geochemical fluxes associated with reverse weathering

Clay mineral reactions, such as smectite-illitization, kaolinization and chloritization, which occur during late burial diagenesis, are often considered to be slow (e.g. Cuadros *et al.*, 2017). In contrast, the formation of authigenic clay minerals in modern marine sediments by reverse weathering reactions is increasingly recognized as a faster process and can therefore influence modern and past ocean chemistry and related element (re)cycling at the sediment–seawater interface (e.g. Baldermann *et al.*, 2022).

The first indications for the substantial removal of Na^+, Mg^{2+} and K^+ ions and $Si(OH)_4$ from present-day seawater by clay mineral authigenesis were provided by Mackenzie & Garrels (1966a). They concluded that element sequestration by reverse weathering balances the riverine influx of the dissolved components from the continents. Since then, extensive field, modelling and laboratory studies have been published that strengthen the evidence for reverse weathering as a key process impacting modern marine element cycles (e.g. Michalopoulos & Aller, 1995; Michalopoulos *et al.*, 2000; Wallmann *et al.*, 2008, 2023; Baldermann *et al.*, 2015; 2022; Ehlert *et al.*, 2016; Cuadros *et al.*, 2017; Geilert *et al.*, 2023). Although the reverse weathering fluxes of individual elements are relatively small (<10%) compared to the global marine carbon and silicon budgets, clay mineral authigenesis can sequester various chemical elements, such as Na, K, Li, Mg, Fe, Al and Si, implying that the varying rates of clay mineral formation during marine diagenesis can impact global element budgets.

Isson & Planavsky (2018) provided quantitative estimates of the significance of reverse weathering on the modern global silica cycle. They calculated that the oceanic Si output fluxes related to chert formation and reverse weathering reactions account for 10.4 and 0.5

Tmol year^{-1}, respectively. The latter flux is equivalent to 4.6% of the total continental Si input to the oceans by combined riverine, hydrothermal, aeolian and groundwater sources (10.9 Tmol year^{-1}). However, Tréguer *et al.* (2021) proposed that the Si output flux due to reverse weathering is much higher than previously calculated, at ~5 Tmol year^{-1}. This 10-fold difference in the calculated Si output flux reflects the problems associated with model parameterization of reverse weathering reactions occurring in the modern oceans.

More recently, Wallmann *et al.* (2023) reported on the modern oceanic element fluxes associated with marine silicate weathering and authigenic clay mineral formation. They calculated net fluxes across the sediment–seawater interface in the order of +1.5 Tmol Na year^{-1}, –2.5 Tmol K year^{-1}, –2.0 Tmol Mg year^{-1}, +2.5 Tmol Ca year^{-1} and +1.9 Tmol Si year^{-1}, where the positive numbers indicate cation release into seawater mainly due to feldspar (e.g. plagioclase) dissolution and the negative numbers denote cation uptake by the precipitation of unspecified authigenic clay minerals and carbonates. However, these estimates did not consider Si burial through biogenic opal precipitation.

More specifically, it has been reported that element sequestration associated with glauconite formation in modern shallow marine settings (0–200 m water depth) sequesters ~0.06 Tmol year^{-1} of K, Mg and Al, ~0.1 Tmol year^{-1} of Fe and ~0.3 Tmol year^{-1} of Si, respectively (see fig. 4 in Baldermann *et al.*, 2022). This is equivalent to ~3–6% of the total oceanic K inventory that is delivered from riverine and hydrothermal sources and thus of the same order of magnitude as the K burial flux attributed to authigenic Fe-illite formation in mangrove forests (up to 0.1 Tmol year^{-1}; Cuadros *et al.*, 2017). Although these estimates have a high degree of uncertainty, Li *et al.* (2022a) proposed that glauconite is an important sink of seawater K (~0.2 Tmol year^{-1}) based on K isotope measurements of modern marine 'bulk' sediments. Regarding the marine Mg cycle, glauconite formation at the marine shelf has been estimated to constitute ~10–38% of the Mg consumption by authigenic clays forming in the

Amazon deltaic sediments (~0.21 Tmol year^{-1}) and ~1–3% of the Mg sink that is associated with fresh oceanic crust alteration (Sun *et al.*, 2016; Huang *et al.*, 2018). Shallow-water glauconite formation may be even more important for the marine Al and Si cycles. It involves ~27–82% removal of the dissolved riverine Al influx entering the modern oceans (~0.1 Tmol year^{-1}; Maring & Duce, 1987) and ~10% removal of the total Si uptake by authigenic clay minerals on a global scale (~4.7 ± 2.3 Tmol year^{-1}; Rahman *et al.*, 2016; Tréguer *et al.*, 2021). In addition, glauconite formation acts as a significant sink for Fe, sequestering ~8–33% of the dissolved and particulate riverine fluxes of Fe that enter the ocean (~0.48–0.86 and ~0.63 Tmol year^{-1}, respectively; Raiswell, 2006).

In contrast, the elemental uptake rates by glauconite formation in modern deep-marine sediments are currently poorly constrained, but Fe sequestration at Ocean Drilling Project (ODP) Site 959 (Ivory Coast–Ghana Marginal Ridge) has been estimated to be ~80 μmol cm^{-2} kyr^{-1}. Although this oceanic sink of Fe is two orders of magnitude lower than that of modern shelf areas, it is (on average) six times higher than that related to the formation of pyrite in suboxic subsurface sediments 5 m below the seafloor or shallower (Baldermann *et al.*, 2015). This indicates that glauconite formation in the deep sea may also act as an important Fe sink, in addition to marine Fe-sulfide minerals, which develop under euxinic to anoxic conditions deeper within the sedimentary pile (e.g. Raiswell & Canfield, 2012). As for the modern deep-sea Al, Si, K and Mg cycles, however, glauconite precipitation seems to be less important, which has been attributed to the slower reaction rates at the lower temperatures (<5°C) of deep-sea settings (e.g. Baldermann *et al.*, 2013, 2015, 2022). However, Logvinenko (1982) has reported that modern deep-sea sediments contain ~1–2 wt.% glauconite or glauconite-smectite on average. In modern calcareous and fossiliferous deep-sea sediments, the glauconite content is even higher, reaching 2–3 wt.% on average, according to Giresse *et al.* (2004) and Wigley & Compton (2007). These relationships may

suggest that the elemental uptake rates of Al, Si, K and Mg by glauconite formation in the deep ocean are currently underestimated.

In hydrothermally influenced sediments, such as at the Galapagos spreading centre, the Mid-Atlantic Ridge, the Crozet Island Archipelago, the Costa Rica Margin, the Pacific–Antarctic Ridge and the Chile Ridge, precipitation of Fe-bearing smectites occurs in the form of nontronite, Fe(III)-montmorillonite and saponite. The formation of these minerals can locally take up ~1000 µmol Fe cm^{-2} kyr^{-1}, suggesting that smectite authigenesis at thermally active sites of the deep sea can also constitute an important (but locally restricted) Fe sink in the modern oceans (e.g. Chester, 2000). Additional reverse weathering reactions occur *via* the low- and high-temperature interaction of fresh oceanic crust and seawater in the vicinity of mid-ocean ridge sites (e.g. Elderfield & Schultz, 1996; Higgins & Schrag, 2015; Voigt *et al.*, 2020). These have been proposed to contribute strongly to the elemental and isotopic composition of seawater, as indicated by *in situ* Rb-Sr dating of celadonite forming within veins and amygdales ~20 Myr after ocean crust accretion (Laureijs *et al.*, 2021a). That study also concluded that widespread celadonite formation occurring in ocean floor sediments and ophiolite lavas could act as an important sink for seawater K (but also Al, Si, Li, B, Mg and Fe), but without providing robust mass balance constraints to support their hypothesis. This could not be achieved due to the incomplete sample recovery associated with ocean-floor drilling and related challenges in quantifying the heterogeneous distribution of K-rich phases in the upper oceanic crust (Laureijs *et al.*, 2021b).

While the influence of reverse weathering on major element cycles is becoming increasingly recognized, especially with regard to often easily extractable (millimetre-sized) and quantifiable glauconite and celadonite grains, there are few constraints on the impacts of reverse weathering on the cycling of minor and trace elements in the ocean (e.g. Tostevin & Ahmed, 2023). This is largely due to the difficulty of separating and purifying typically

micrometre-scale authigenic clay minerals, which are usually closely intergrown with detrital clay minerals of similar size. It has been proposed, based on porewater analyses, that the modern marine rare earth element (*REE*) cycle is largely controlled by the balance of *REE* release from detrital clay mineral dissolution *versus* uptake of *REEs* by authigenic clay minerals, Fe/Mn-(hydr)oxides and phosphates (e.g. Abbott *et al.*, 2019). Recent analyses of authigenic glauconite separates from the West African continental margin and comparison to the detrital clay mineral-rich muds in which they form support this model (Bayon *et al.*, 2023), whereby detrital clay mineral dissolution coupled with *REE* uptake by marine authigenic clay minerals is responsible for the large sedimentary flux of *REEs* in the modern oceans (e.g. Abbott *et al.*, 2015, 2019; Haley *et al.*, 2017). In addition, the work of Bayon *et al.* (2023) suggests that glauconite formation from a detrital clay mineral precursor assemblage is associated with net sinks of Mo, Cr, V and Rb but represents a source of U, Li, Co, Ni, Hf, Zr, Th and Ba. Similarly, authigenic smectites in a Cenozoic sequence from the Ross Sea (Antarctica) have been reported to be enriched in V, Cr, Co, Ni and Sc compared to co-occurring detrital clay minerals (Setti *et al.*, 2004). Other recent work suggests that authigenic clay mineral formation may act as a Be sink (Bernhardt *et al.*, 2020). In addition, clay mineral synthesis experiments suggest that greenalite may have been an important sink of Cu, V and Zn in the Precambrian oceans (Tostevin & Ahmed, 2023).

Isotope proxies used to trace clay mineral reactions

The development of multi-collector inductively coupled plasma mass spectrometry (MC-ICP-MS) and thermal ionization mass spectrometry (TIMS) marked a significant step towards the improved measurement of the isotopic composition of minerals. These instruments are used to accurately measure elements and their isotopes down to ppm and ppb concentrations with light to large atomic masses (Li, B *versus* Ca, Fe, Mg, Sr, Zn, *etc*.) in a suite of components, such as carbonates, phosphates and silicates. These analytical techniques allowed the

establishment of a range of new tools and proxy signals to identify and quantify (bio)geochemical processes occurring in Earth's (surface) settings, such as chemical weathering reactions, element cycles and fluid–mineral interactions (e.g. Pogge von Strandmann *et al.*, 2008; Oelkers *et al.*, 2015; Schott *et al.*, 2016; Andrews *et al.*, 2020; Chanda *et al.*, 2023; Farkaš *et al.*, 2025). While the elemental and isotopic compositions of carbonates have long been used to reconstruct conditions prevailing at the time of their formation (i.e. palaeo-pH, temperature, redox conditions and growth rate), and thus seawater chemistry over time (e.g. Kampschulte & Strauss, 1998; Eiler, 2007), applying such methods to determine palaeo-environmental information from authigenic and detrital clay minerals is less well established. This is, among other factors, due to: (1) the lack of well-constrained fractionation factors for clay mineral–fluid systems and substantial isotopic differences between adsorbed/exchangeable and structurally incorporated constituents (e.g. Köster *et al.*, 2019; Li *et al.*, 2022a); (2) the difficulties in synthesizing well-crystallized and close to pure clay minerals at ambient temperature (e.g. Kloprogge, 1998; Baldermann *et al.*, 2024); and (3) the challenges associated with isolating authigenic clay minerals from phyllosilicates of detrital origin (e.g. Zhang *et al.*, 2010; Tosca & Masterson, 2014; Han *et al.*, 2022a, 2024; Bayon *et al.*, 2023).

Nevertheless, field and experimental studies using the isotopic composition of clay minerals to reconstruct marine element cycles and weathering/alteration pathways occurring in various sedimentary environments are currently on the increase. This is because marine authigenic clay minerals (1) are probably more resistant to post-depositional alteration compared to the more reactive carbonates, (2) incorporate more elements of interest (e.g. K, Si and Li) and in greater abundance than carbonates (which may also be affected by as-yet unknown vital effects), allowing for the development of more new proxies (Li *et al.*, 2022a, 2022b), (3) represent important sinks for many elements, meaning that the isotopic characterization of

authigenic clay minerals can potentially better constrain modern and past marine elemental budgets *via* isotope mass balance approaches (e.g. Zheng *et al.*, 2022), and (4) are datable through conventional K-Ar and ^{40}Ar-^{39}Ar analysis or advanced *in situ* Rb-Sr analysis by laser ablation collision cell inductively coupled plasma mass spectrometry (LA-ICP-MS/MS; e.g. Kelley, 2002; Clauer *et al.*, 2012; Hogmalm *et al.*, 2017; Scheiblhofer *et al.*, 2022). This is particularly the case for glauconite, for which new isotope proxies are actively being developed (Fig. 9), taking advantage of the relative ease with which typically millimetre-sized glauconite pellets can be separated from their host sediments and purified using standard sieving, acid leaching and magnetic separation techniques or can be directly targeted for *in situ* analyses.

$$(K,Na,Ca)_{\sim 0.6-0.8}(Fe^{3+/2+},Al,Mg)_{\sim 2}[(Si,Al)_4]O_{10}(OH)_2$$

δ^{56}Fe: redox, source
δ^{24}Mg: seawater, weathering, kinetics
δ^{66}Zn: redox, source, pH
δ^{7}Li: weathering, source

δ^{41}K: seawater, weathering
δ^{44}Ca: biology, kinetics
^{87}Sr/^{86}Sr: seawater
+
K-Ar, ^{40}Ar-^{39}Ar, Rb-Sr, K-Ca: age dating

δ^{30}Si: biology, concentration, kinetics, crystallization
δ^{11}B: fluid source, pH
δ^{18}O/ δD: temperature, source, evaporation
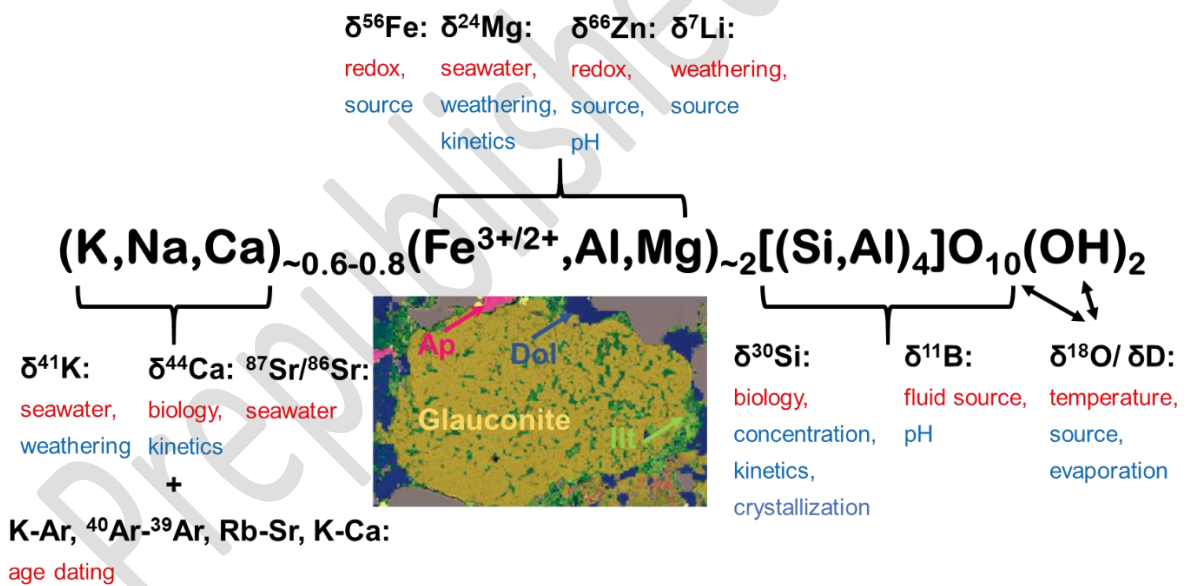
Figure 9. Illustration showing potential environmental geochemical and isotopic proxies recorded in glauconite and surrounding sediments. Red text indicates primary proxies of high significance; blue text indicates secondary proxies of lower significance (i.e. these are often influenced by other environmental controls and therefore difficult to interpret). Ap = apatite; Dol = dolomite; Ilt = illite

Clay minerals, as hydrous phyllosilicates, contain water (i.e. $\delta^{18}O$ and δD isotopic systems) that can be (1) adsorbed on the external surface sites, (2) weakly bound in the interlayer sheet in the case of swellable clay minerals and (3) more strongly bound as hydroxyls in the octahedra. Whereas the first two types of water can isotopically exchange with ambient fluids within minutes to days, structurally bound water frequently shows slow isotope exchange rates depending on temperature and the type of clay mineral (e.g. Clauer *et al.*, 2014). Importantly, the re-equilibration of H isotopes takes place faster at lower temperatures than that of O isotopes, so that the $\delta^{18}O$ and δD signatures of clay minerals can provide insights into the nature of mineral reactions (e.g. Schön *et al.*, 2016). For example, the temperature of smectite formation, its post-depositional (re)equilibration/transformation into illite and the kinetics of isotopic exchange between glauconite, host sediment and pore fluid can be resolved (e.g. Savin & Epstein, 1970).

Stable silicon isotopes ($\delta^{30}Si$) offer a sensitive proxy for studying dissolution–precipitation reactions of silicate minerals in marine sediments (e.g. Rahman *et al.*, 2017). Light Si isotopes (^{28}Si) are preferentially taken up over heavy Si isotopes (^{30}Si) from the pore fluid during precipitation of authigenic clay minerals, shifting pore fluid $\delta^{30}Si$ to higher values, often exceeding seawater values (e.g. Ehlert *et al.*, 2016; Geilert *et al.*, 2023). Elevated pore fluid $\delta^{30}Si$ is thus commonly inferred to reflect authigenic clay mineral formation. However, present constraints on marine authigenic clay mineral $\delta^{30}Si$ derive almost entirely from sequential leaching approaches (e.g. Pickering *et al.*, 2020; Huang *et al.*, 2023), with inherent ambiguity related to the potential dissolution of non-target phases, such as detrital clay minerals. Alternative estimates of authigenic clay mineral $\delta^{30}Si$ based on isotope mass balance are helpful (e.g. Rahman & Trower, 2023) but are impacted by uncertainties in the present-day marine Si cycle. More direct constraints from *in situ* laser ablation analysis of

authigenic clay minerals (e.g. Geilert *et al.*, 2023) or conventional solution-based analyses of authigenic clay mineral separates (e.g. glauconite pellets; Geilert *et al.*, 2024) have the potential to substantially reduce these uncertainties and therefore greatly improve quantification of benthic Si fluxes, alkalinity and cation budgets related to marine silicate alteration (e.g. Wallmann *et al.*, 2008; 2023; Geilert *et al.*, 2024; Farkaš *et al.*, 2025). For example, the δ^{30}Si signatures of a bulk sediment rich in diatoms, its porewater, the terrigenous fraction and the authigenic Fe-smectite or glauconite-smectite, obtained by laser ablation, were recently used to demonstrate rapid marine silicate alteration and related clay mineral formation during a coastal El Niño extreme weather event at the Peruvian margin (Geilert *et al.*, 2023). This case study illustrated the fact that clay mineral authigenesis can impact the marine element cycle and the CO_2 cycle on timescales of weeks to months.

The fractionation behaviour of boron isotopes (δ^{11}B) of clay minerals depends on temperature, B speciation, fluid δ^{11}B composition, pH, fluid/rock ratio and (re)equilibration time between the solid and fluid phase (e.g. Williams *et al.*, 2001; Deyhle & Kopf, 2005). Boron isotopes have been used for reconstructing the fluid source(s) involved in the formation of ash-derived bentonite deposits in marine and terrestrial low-temperature environments (e.g. Köster *et al.*, 2019; Clauer *et al.*, 2022). Moreover, B concentrations and δ^{11}B signatures of diagenetically modified and rejuvenated glauconites can record either ancient seawater δ^{11}B composition or incorporation of organic-derived light ^{10}B into glauconite during diagenesis, which enables reconstruction of the evolutionary history of glauconite (Środoń *et al.*, 2023).

Another isotope system that has seen great interest in recent years is the stable potassium system (δ^{41}K; e.g. Farkaš *et al.*, 2025). The balance between silicate weathering and marine clay mineral authigenesis acts as an important control on Earth's long-term carbon cycle. Since these processes also represent important influences on the marine K cycle (e.g. Li *et*

al., 2022a) and are thought to be associated with substantial K isotopic fractionations (e.g. Li *et al.*, 2019b, 2021c; Teng *et al.*, 2020), the δ^{41}K signature of seawater has the potential to become an important new tool for understanding long-term changes to the carbon cycle (e.g. Li *et al.*, 2019c; Hu *et al.*, 2020). Preferential uptake of the lighter K isotope (^{39}K) during authigenic clay mineral formation or during adsorption processes by clay minerals in the marine sediment is likely to be a key factor explaining the surprisingly heavy isotopic composition of present-day seawater (~0.12‰ ± 0.07‰), considering the K isotope difference between modern seawater and Bulk Silicate Earth of ~0.6‰ (e.g. Li *et al.*, 2022a). The large K isotopic difference between seawater and Earth's silicate crust (i.e. upper continental crust; –0.44‰ ± 0.05‰; Huang *et al.*, 2020) remains enigmatic because modern seawater shows a significant excess of the heavy ^{41}K isotope compared to the main input fluxes of K into the ocean. We note, however, that no direct measurements of modern or recent authigenic clay mineral δ^{41}K have been published to date (only from bulk sediment), which is due to the difficulties in isolating these authigenic clay minerals from the host sediment. However, pellet-forming authigenic clay minerals, such as glauconite and celadonite (e.g. Santiago Ramos *et al.*, 2020), are promising targets and have the potential to become an important archive for the reconstruction of seawater δ^{41}K changes over time. Alternative sedimentary archives, which may also record seawater δ^{41}K, include biogenic carbonates and K-rich evaporite salts, but these are either convoluted by vital effects and low K contents or show a very patchy temporal distribution (e.g. Li *et al.*, 2022a). Direct measurement of authigenic clay mineral δ^{41}K is thus a key research priority that can be used to assess the relative impact on seawater δ^{41}K caused by changes in continental weathering intensity (e.g. Hu *et al.*, 2020; Li *et al.*, 2022a), the rates of low-temperature seafloor alteration and the magnitude of authigenic clay mineral formation in marine sediments (e.g. Wang *et al.*, 2021).

We have already mentioned the important role of reverse weathering in the marine *REE* budget, with the sedimentary *REE* fluxes and the related composition of the marine bottom waters being controlled by the dissolution of detrital clay minerals *versus* the uptake of *REEs* by authigenic clay minerals (e.g. Haley *et al.*, 2017; Abbott *et al.*, 2019; Bayon *et al.*, 2023). This has important implications for the *REE* concentration and the Nd isotopic composition of water masses, which have been shown to evolve over distance, location and time (e.g. Abbott *et al.*, 2019). It has been proposed that authigenic clay minerals, such as glauconite, may be promising recorders of bottom water or porewater Nd isotopic compositions (e.g. Giresse *et al.*, 2021), with potential applications for reconstructing changes to ocean circulation over time. Similarly, radiogenic Sr isotope ($^{87}Sr/^{86}Sr$) signatures have been used to track the evolution of authigenic clay minerals, showing that $^{87}Sr/^{86}Sr$ of detrital clay minerals is progressively lost as they are replaced by authigenic clay minerals, causing $^{87}Sr/^{86}Sr$ to approach a composition that is more similar to that of seawater (e.g. Clauer *et al.*, 1992). This observation is also commonly used to justify anchoring of Rb-Sr isochrons using expected seawater Sr isotope values (e.g. Redaa *et al.*, 2023).

Other promising isotope systems that have only rarely been applied to marine authigenic clay minerals include (1) magnesium ($\delta^{26}Mg$) and calcium ($\delta^{44}Ca$) for obtaining insights into biogeochemically coupled processes, weathering rates and marine element budgets (e.g. Dunlea *et al.*, 2017; Huang *et al.*, 2024), (2) lithium ($\delta^{7}Li$) to quantify continental palaeo-weathering regimes *versus* rates of oceanic crust alteration (e.g. Zhang *et al.*, 2022a; Yin *et al.*, 2023) and (3) zinc ($\delta^{66}Zn$), iron ($\delta^{56}Fe$) and chromium ($\delta^{53}Cr$) to constrain palaeo-redox conditions during clay mineral precipitation (cf. Fig. 9).

Another (re)emerging application for authigenic clay minerals that is likely to gain importance aims to determine the absolute depositional ages of marine sedimentary rocks. The most widely used radiometric techniques for obtaining absolute depositional ages are

presently U-Pb zircon dating of volcanic ash (e.g. Linnemann *et al.*, 2018), ^{40}Ar/^{39}Ar dating of lava flows (e.g. Jourdan *et al.*, 2005) and Re-Os dating of organic-rich black shales (e.g. Rooney *et al.*, 2015; Millikin *et al.*, 2022). Because these target lithologies are often restricted to specific tectonic or environmental settings, dating sedimentary sequences remains among the most challenging tasks in geochronology. Glauconite geochronology is a potential alternative approach where ash beds or black shales are absent. In fact, ~40% of all ages used to constrain the geological timescale of the last 250 Myr up until the mid-1990s were obtained from glauconite (Smith *et al.*, 1998). Although glauconite bulk separates have long been dated using the Rb-Sr, K-Ca, K-Ar and ^{40}Ar-^{39}Ar techniques, frequent mismatches with independent chronostratigraphic constraints (e.g. Selby, 2009; Cecil & Ducea, 2011) mean that glauconite geochronology is no longer widely employed. Erroneous ages have been attributed to factors including the presence of detrital Rb- and K-bearing phases in glauconite separates, the presence of younger and isotopically distinct clay mineral overgrowths, as well as post-depositional disruption or resetting of the Rb-Sr isotope system by exposure to increased temperatures and/or fluid–rock interactions (e.g. Rafiei *et al.*, 2023). Various sample preparation and screening approaches, based on improved mineral separation and more aggressive chemical cleaning, have been developed to address these problems, but with varying degrees of success (e.g. Derkowski *et al.*, 2009).

The advent of *in situ* Rb-Sr and K-Ca dating offers a promising new approach that has the potential to resolve many of these limitations, leading to a recent revival in authigenic clay mineral-based geochronology (e.g. Zack & Hogmalm, 2016; Hogmalm *et al.*, 2017; Laureijs *et al.*, 2021a; Redaa *et al.*, 2023). Unlike traditional solution-based Rb-Sr dating, which requires the dissolution of bulk sample powders followed by wet chemical separation of Rb and Sr, reaction cell mass spectrometry resolves the spectral overlap of, for example, ^{87}Rb and ^{87}Sr *via* the addition of a reaction gas (e.g. N$_2$O) to a reaction cell (e.g. Hogmalm *et al.*,

2017; Gorojovsky & Alard, 2020; Redaa *et al.*, 2023). In the case of the Rb-Sr system, Rb is measured based on mass while Sr isotopes are measured as mass-shifted oxides (i.e. produced by reaction with the gas), allowing quantitative online separation of ^{87}Rb and ^{87}Sr. When combined with recent advances in sedimentary petrography (Rafiei *et al.*, 2020; Han *et al.*, 2022a) this approach permits rapid *in situ* Rb-Sr dating of carefully screened glauconite or celadonite grains, which opens up a range of new applications (e.g. Laureijs *et al.*, 2021a; Scheiblhofer *et al.*, 2022; Rafiei *et al.*, 2023; Redaa *et al.*, 2023). For Precambrian mudrocks rich in authigenic clay minerals, *in situ* dating of marine authigenic illite has also shown great promise (e.g. Subarkah *et al.*, 2022, 2024).

Clay minerals in geoengineering: porewater alkalinity enhancement

A major challenge facing today's society is to limit anthropogenically induced global warming to 1.5°C above the pre-industrial value (e.g. United Nations Framework Convention on Climate Change, 2015). As a result, various strategies for CO_2 removal at an industrial scale have been proposed over the past three to four decades, such as carbon capture and storage or carbon capture and utilization methods.

A novel and sustainable solution to decrease atmospheric CO_2 concentrations is to bind carbon in near-surface marine sediments and directly in the oceans (e.g. Morrow *et al.*, 2020; Meier *et al.*, 2022) by enhancing the chemical weathering rates of silicates and the resulting alkalinity of marine porewaters (e.g. Bellamy *et al.*, 2012; Bach *et al.*, 2019; Fakhraee *et al.*, 2023; Hartmann *et al.*, 2023; Iglesias-Rodríguez *et al.*, 2023; Dale *et al.*, 2024; Marín-Samper *et al.*, 2024). As described earlier, silicate mineral weathering achieves this by releasing cations and binding CO_2 (i.e. HCO_3^- and CO_2^{2-} ions), thus facilitating the uptake of atmospheric CO_2 by the ocean (e.g. Feng *et al.*, 2017). The spreading of crushed mafic rocks, such as basalt, and mafic minerals (here: forsterite, Mg_2SiO_4) in marine settings is increasingly considered in geoengineering to stabilize Earth's climate through long-term

binding and storage of atmospheric CO_2 following Equation 10 (e.g. Wood & Kleppa, 1981; Taylor *et al.*, 2016):

$$Mg_2SiO_4 + 4CO_2 + 4H_2O \rightarrow 2Mg^{2+} + 4HCO_3^- + Si(OH)_4 \qquad (10)$$

During this irreversible dissolution reaction, 1 mol of olivine sequesters 4 mol of CO_2, releasing stoichiometric amounts of HCO_3^- and dissolved metal (cat)ions to the marine pore fluid. However, this process can subsequently trigger marine clay mineral authigenesis and hence reverse weathering (Fig. 10). Depending on the species formed and the reaction pathway, these reactions may lead to the recycling or release of CO_2, meaning that the net carbon mass balance remains unknown. Although such a CO_2 sequestration technique still requires verification and optimization of the total CO_2 binding capacity at individual test sites, as well as estimation of the costs and potential environmental risks, this approach has great potential for application on a large scale (e.g. Montserrat *et al.*, 2017).

Based on CO_2 mass balance calculations (Equation 10), olivine deployments in high-energy marine–coastal environments have been proposed (e.g. Meysman & Montserrat, 2017). On main shipping routes, olivine release from vessel tanks is currently under consideration in the open ocean (e.g. Köhler *et al.*, 2013). Laboratory and modelling studies have demonstrated the great potential of alkalinity enhancement by chemical weathering of silicates, with recognition of mineral-specific CO_2 uptake rates, nutrient release rates and ecological effects (e.g. Monserrat *et al.*, 2017; Bach *et al.*, 2019; Fuhr *et al.*, 2022).

Despite the significant interest, field-scale experiments in marginal marine environments (under natural conditions) are still scarce, and the counteracting role of any reverse weathering reaction (e.g. Wallmann *et al.*, 2023) remains largely unknown. In a recent study, He & Tyka (2023) proposed that at favourable near-coastal sites, such as in north Madagascar, California, Brazil, Peru and locations close to the Southern Ocean, a carbon

uptake efficiency of ~0.6–0.8 mol CO_2 per mol of alkalinity could be reached after 3–4 years. Moreover, Mendes *et al.* (unpublished data) are currently conducting alkalinity enhancement experiments by deploying picro-basalt and basanite in the pioneer vegetation zone of salt marshes in Portugal and monitoring their impacts on the ecosystem and porewater chemistry (Fig. 10). Preliminary results indicate that: (1) porewater alkalinity increases by a factor of three within a few days of the deployments, maintaining an alkalinity that is ~10–20% higher compared to that at control sites (without deployments) after 6 months; and (2) the release of dissolved $Si(OH_4)$, Mg^{2+} and Fe^{2+} ions from olivine, pyroxene and feldspar dissolution triggers the formation of smectite at as-yet unknown rates, confirming the importance of reverse weathering reactions in marine settings (e.g. Han *et al.*, 2022b; Mendes *et al.*, unpublished data).
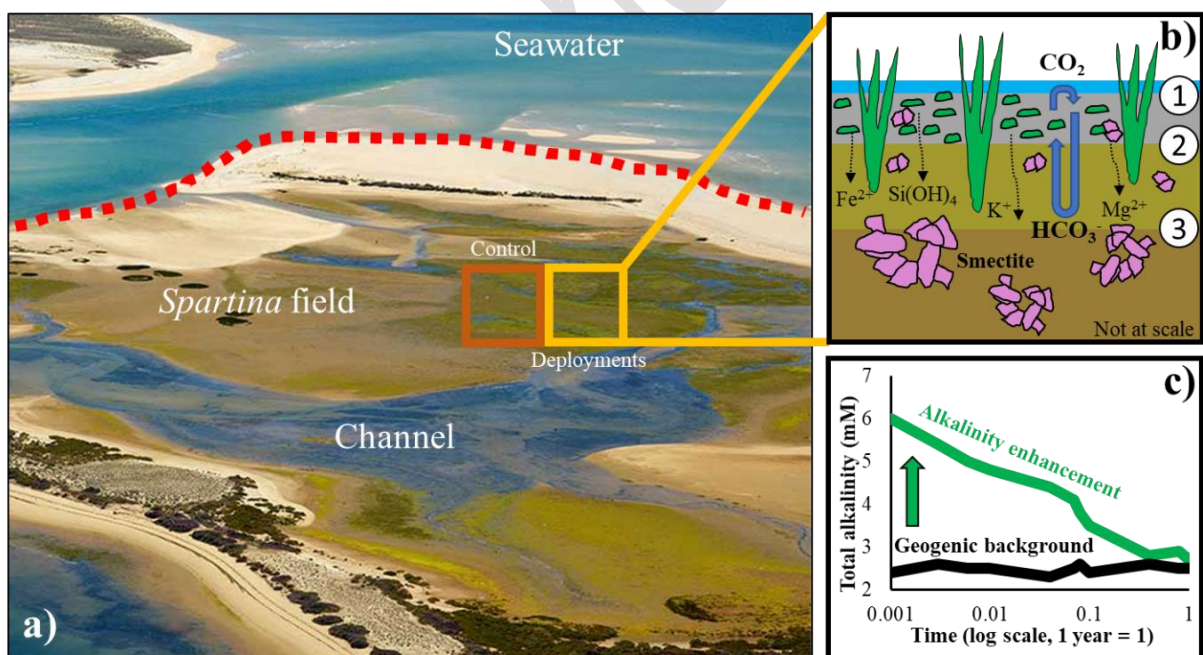
Figure 10. (a) Field-scale (carbonate) alkalinity enhancement test site situated in the pioneer vegetation zone of salt marshes in Portugal. (b) Illustration showing mineral reactions and element transfer at the interface between (1) seawater and substrate (deployment: reactive

mafic rock rich in olivine), (2) substrate and biologically active top layer and (3) top layer and marsh sediments. Olivine dissolution consumes CO_2 and liberates carbonate alkalinity and elements, causing smectite formation. (c) Evolution of the alkalinity profiles in sediment porewater with time at control sites without deployments (marked by the geogenic background curve with a low alkalinity) and at deployment sites (marked by the green curve with a ~2.5-fold higher alkalinity due to enhanced olivine weathering). Note that the deployment sites approach the geogenic background alkalinity level in a relatively short timeframe, which suggests that reverse weathering takes place (i.e. CO_2 release).

However, before this type of geoengineering can be applied to marine settings on a larger scale (e.g. gigaton scale; He & Tyka, 2023), potential side effects and consequences have to be identified and carefully monitored, such as: (1) the formation of distinct chemical and microbial environments on deployed mineral particles and grain surfaces; (2) the response of the biological community to the nutrients released by the deployments; (3) the evolution of porewater geochemistry; (4) the long-term links between increased carbonate alkalinity, porewater pH and carbonate mineral saturation indices; (5) the rate of CO_2 re-equilibration with the atmosphere; and (6) the impact of smectite authigenesis on the physicochemical properties of the marine sediment (e.g. Simon *et al.*, 2002; van der Jagt *et al.*, 2018; Hartmann *et al.*, 2023).

Clay minerals as slow-release fertilizers

Clay minerals that formed during continental chemical weathering, as well as during reverse weathering, are increasingly being used in agriculture for soil conditioning and soil environmental improvement. The addition of these minerals helps mitigate the accumulation of excess nutrients in soils and water bodies worldwide caused by the application of

conventional, easily soluble (K-N-P-based) fertilizers. The overuse of common fertilizers leads to burning or nitrate poisoning of plants and to the increased eutrophication of freshwater bodies, as well as to increased emissions of the greenhouse gas nitrous oxide. Hence, modern agricultural practices focus on the efficient use of sustainable 'green' fertilizer technologies (e.g. Tilman *et al.*, 2001). One solution to this challenge is the use of functional fertilizers, which enable the controlled or slow release of nutrients (e.g. Sharma, 1979; Liu *et al.*, 2022). Slowly dissolving silicate-based fertilizers, such as glauconite (or greensand), aim to deliver nutrients to plants in a targeted (and directed) manner, thus increasing crop yields while reducing environmental pollution. These controlled-release products typically consist of nutrients (e.g. N, P or other macro- and micronutrients) that are loaded onto a clay mineral-based carrier (e.g. glauconite), whose properties determine the release rate of the nutrients (e.g. Fu *et al.*, 2018; Rahman *et al.*, 2021; Duan *et al.*, 2023; Moradi *et al.*, 2023). Moreover, it has been found that, in the long term, additional secondary clay mineral assemblages may form, such as ferruginous smectite, illite-smectite and metal (hydr)oxides (e.g. Pestitschek *et al.*, 2012), which help to maintain the favourable physicochemical properties of the soil, such as a greater pH buffer capacity, an elevated organic matter content and increased water retention and ion-exchange capacities (e.g. Li *et al.*, 2019a).

Clay minerals such as smectites (e.g. Pereira *et al.*, 2015; Ren *et al.*, 2024), kaolinite (e.g. Lei *et al.*, 2018; AlShamaileh *et al.*, 2022), halloysite (e.g. Maximov *et al.*, 2023) and glauconite (e.g. Vakal *et al.*, 2020; Rudmin *et al.*, 2023b) have been investigated in the search for cost-effective and environmentally friendly nutrient-carrier materials. Current research has focused on glauconite because this mineral can act as a carrier for nitrogen (N) and as a natural source of K. For example, glauconite loaded with ammonium (NH_4^+) ions, carbamide (urea) or ammonium dihydrogen phosphate has been proposed as a promising slow-release fertilizer (e.g. Rudmin *et al.*, 2023b). It was found that the adsorption of NH_4^+ ions into the

micropores of glauconite or in the interlayer sites of smectite within interstratified glauconite-smectite occurs immediately after the preparation of the mixtures. It was suggested that the degree of NH_4^+ adsorption by globular glauconite depends on the distribution and abundance of surface-accessible pores and on the smectite content. Importantly, such glauconite fertilizers exhibited prolonged release times for N and K, making them suitable for diverse slow-release fertilizing purposes (e.g. Rudmin *et al.*, 2023b). These findings advance our understanding of the influence of environmental conditions on reverse weathering. Future studies should make use of isotopes to quantify the rates of silicate weathering *versus* near-surface clay mineral neoformation and also explore how the application of large volumes of slow release clay-based fertilizers to soils may eventually, after chemical degradation and transport, impact reverse weathering processes in marine environments.

Conclusion and perspectives

Reverse weathering processes produce a suite of authigenic clay minerals in marine sediments over comparatively short geological timescales. Despite the generally sluggish reaction kinetics of near-surface clay mineral authigenesis, there is increasing evidence from modelling, isotopic and experimental studies for the occurrence of faster reactions and substantial element sequestration (K, Si, Mg, *REEs*, Li, B, *etc*.) associated with reverse weathering. This takes place in shallow-marine and deep-marine depocentres, as well as in marine hydrothermal surroundings. A complex interplay occurs between global climate change and elemental fluxes to the oceans, which are intimately related to the rates of continental and seafloor chemical weathering, the evolution of seawater biogeochemistry and elemental uptake fluxes associated with marine clay mineral sinks. Novel analytical approaches used to quantify clay mineral reactions are advancing, which will allow better estimations of the efficiency of reverse weathering. These advances are driving applications and proposals for clay mineral-related geoengineering for CO_2 sequestration and for slow-

release fertilizers as soil amendments. However, further progress in understanding the links between silicate weathering and reverse weathering is needed, which requires continued field studies, advanced laboratory approaches and numerical modelling. Such advancement underlines the great relevance of reverse weathering reactions on past and present marine element cycles and Earth's climate.

Conflicts of interest

The authors declare none.

References

Abbott A.N., Haley B.A., McManus J. & Reimers C.E. (2015) The sedimentary flux of dissolved rare earth elements to the ocean. *Geochimica et Cosmochimica Acta*, **154**, 186–200.

Abbott A.N., Löhr S. & Trethewy M. (2019) Are clay minerals the primary control on the oceanic rare earth element budget? *Frontiers in Marine Sciences*, **6**, 504.

Afify A.M., Sanz-Montero M.E. & Calvo J.P. (2015) Ironstone deposits hosted in Eocene carbonates from Bahariya (Egypt) – new perspective on cherty ironstone occurrences. *Sedimentary Geology*, **329**, 81–97.

Afify A.M., Sanz-Montero M.E. & Calvo J.P. (2018) Differentiation of ironstone types by using rare earth elements and yttrium geochemistry – a case study from the Bahariya region, Egypt. *Ore Geology Reviews*, **96**, 247–261.

Akbulut A. & Kadir, S. (2003) The geology and origin of sepiolite, palygorskite and saponite in Neogene lacustrine sediments of the Serinhisar-Acipayam Basin, Denizli, SW Turkey. *Clays and Clay Minerals*, **51**, 279–292.

AlShamaileh E., Alrbaihat M., Moosa I., Abu-Afifeh Q., Al-Fayyad H., Hamadneh I. & Al-Rawajfeh A. (2022) Mechanochemical preparation of a novel slow-release fertilizer based on K_2SO_4-kaolinite. *Agronomy*, **12**, 3016.

Altschuler Z.S., Dwornik E.J. & Kramer H. (1963) Transformation of montmorillonite to kaolinite during weathering. *Science*, **141**, 148–152.

Andrews A.J. (1980) Saponite and celadonite in layer 2 basalts, DSDP Leg 37. *Contributions to Mineralogy and Petrology*, **73**, 323–340.

Andrews E., Pogge von Strandmann P.A.E. & Fantle M.S. (2020) Exploring the importance of authigenic clay formation in the global Li cycle. *Geochimica et Cosmochimica Acta*, **289**, 47–68.

Armelenti G., Goldberg K., Kuchle J. & de Ros L.F. (2016) Deposition, diagenesis and reservoir potential of non-carbonate sedimentary rocks from the rift section of Campos Basin, Brazil. *Petroleum Geoscience*, **22**, 223–239.

Aubineau J., El Albani A., Bekker A., Fru E.C., Somogyi A., Medjoubi K. *et al.* (2020) Trace element perspective into the ca. 2.1-billion-year-old shallow-marine microbial mats from the Francevillian Group, Gabon. *Chemical Geology*, **543**, 119620.

Aubineau J., El Albani A., Bekker A., Somogyi A., Bankole O.M., Macchiarelli R. *et al.* (2019) Microbially induced potassium enrichment in Paleoproterozoic shales and implications for reverse weathering on early Earth. *Nature Communications*, **10**, 1–9.

Bach L.T., Gill S.J., Rickaby R.E.M, Gore S. & Renforth P. (2019) CO_2 removal with enhanced weathering and ocean alkalinity enhancement: potential risks and co- benefits for marine pelagic ecosystems. *Frontiers in Climate*, **1**, 7.

Bailey S.W. (1988) Odinite, a new dioctahedral-trioctahedral Fe^{3+}-rich 1:1 clay mineral. *Clay Minerals*, **23**, 237–247.

Baioumy H., Farouk S. & Al-Kahtany K. (2020) Paleogeographic, paleoclimatic and sea-level implications of glauconite deposits in Egypt: a review. *Journal of African Earth Sciences*, **171**, 103944.

Baker L.L., Rember W.C., Sprenke K.F. & Strawn D.G. (2012) Celadonite in continental flood basalts of the Columbia River Basalt Group. *American Mineralogist*, **97**, 1284–1290.

Baldermann A., Banerjee S., Czuppon G., Dietzel M., Farkaš J., Löhr S. *et al.* (2022) Impact of green clay authigenesis on element sequestration in marine settings. *Nature Communications*, **13**, 1527.

Baldermann A., Grathoff G.H. & Nickel C. (2012) Micromilieu-controlled glauconitization in fecal pellets at Oker (central Germany). *Clay Minerals*, **47**, 513–538.

Baldermann A., Mavromatis V., Frick P.M. & Dietzel M. (2018) Effect of aqueous Si/Mg ratio and pH on the nucleation and growth of sepiolite at 25 °C. *Geochimica et Cosmochimica Acta*, **227**, 211–226.

Baldermann A., Stamm F.M., Farkaš J., Löhr S., Ratz B., Letofsky-Papst I. & Dietzel M. (2024) Precipitation of short-range order hydroxy aluminosilicate (HAS) and hydrous ferric silicate (HFS) at ambient temperature: insights into mineral formation pathways, crystal chemistry and solubility–stability relationships. *Chemical Geology*, **646**, 121911.

Baldermann A., Warr L.N., Grathoff G.H. & Dietzel M. (2013) The rate and mechanism of deep-sea glauconite formation at the Ivory Coast–Ghana marginal ridge. *Clays and Clay Minerals*, **61**, 258–276.

Baldermann A., Warr L., Letofsky-Papst I. & Mavromatis V. (2015) Substantial iron sequestration during green-clay authigenesis in modern deep-sea sediments. *Nature Geoscience*, **8**, 885–889.

Baldermann A., Wasser O., Abdullayev E., Bernasconi S., Löhr S., Wemmer K. *et al.* (2021) Palaeo-environmental evolution of Central Asia during the Cenozoic: new insights from the continental sedimentary archive of the Valley of Lakes (Mongolia). *Climate of the Past*, **17**, 1955–1972.

Banerjee S., Bansal U. & Thorat A. (2016) A review on palaeogeographic implications and temporal variation in glaucony composition. *Journal of Palaeogeography*, **5**, 43–71.

Banerjee S., Choudhury T.R., Saraswati P.K. & Khanolkar S. (2020) The formation of authigenic deposits during Paleogene warm climatic intervals: a review. *Journal of Palaeogeography*, **9**, 27.

Banerjee S., Jeevankumar S. & Eriksson P.G. (2008) Mg-rich ferric illite in marine transgressive and highstand systems tracts: examples from the Paleoproterozoic Semri Group, central India. *Precambrian Research*, **162**, 212–226.

Banerjee S., Mondal S., Chakraborty P.P. & Meena S.S. (2015) Distinctive compositional characteristics and evolutionary trend of Precambrian glaucony: example from Bhalukona Formation, Chhattisgarh Basin, India. *Precambrian Research*, **271**, 33–48.

Banfield J.F., Jones B.F. & Veblen D.R. (1991) An AEM-TEM study of weathering and diagenesis, Abert Lake, Oregon: II. Diagenetic modification of the sedimentary assemblage. *Geochimica et Cosmochimica Acta*, **55**, 2795–2810.

Bansal U., Banerjee S., Chauhan G., Rudmin M., Borgohain D. & Upadhyay A. (2021) Geochemistry of Callovian ironstone in Kutch and its stratigraphic implications. Pp. 215–239 in: *Mesozoic Stratigraphy of India* (S. Banerjee & S. Sarkar, editors). Society of Earth Scientists Series. Springer Nature, Berlin, Germany.

Bansal U., Banerjee S., Pande K. & Ruidas D.K. (2020) Unusual seawater composition of the Late Cretaceous Tethys imprinted in glauconite of Narmada basin, central India. *Geological Magazine*, **157**, 233–247.

Bayon G., Giresse P., Chen H., Rouget M.-L., Gueguen B., Moizinho G.R. *et al.* (2023) The behavior of rare earth elements during green clay authigenesis on the Congo Continental Shelf. *Minerals*, **13**, 1081.

Bellamy R., Chilvers J., Vaughan N.E. & Lenton T.M. (2012) A review of climate geoengineering appraisals. *WIREs Climate Change*, **3**, 597–615.

Berner R.A. (1990) Atmospheric CO_2 levels over Phanerozoic time. *Science*, **249**, 1382–1386.

Berner R.A., Lasaga A.C. & Garrels R.M. (1983) The carbonate–silicate geochemical cycle and its effect on atmospheric carbon dioxide over the past 100 million years. *American Journal of Science*, **283**, 641–683.

Bernhardt A., Oelze M., Bouchez J., von Blanckenburg F., Mohtadi M., Christl M. & Wittmann H. (2020) $^{10}Be/^9Be$ ratios reveal marine authigenic clay formation. *Geophysical Research Letters*, **47**, e2019GL086061.

Bhattacharyya D.P. (1983) Origin of berthierine in ironstones. *Clays and Clay Minerals*, **31**, 173–182.

Blake R.L. (1965) Iron phyllosilicates of the Cuyuna district in Minnesota. *American Mineralogist*, **50**, 148–169.

Bouna L., Rhouta B., Daoudi L., Maury F., Amjoud M., Senocq F. *et al.* (2012) Mineralogical and physico-chemical characterizations of ferruginous beidellite-rich clay from Agadir Basin (Morocco). *Clays and Clay Minerals*, **60**, 278–290.

Brantley S.L., Shaughnessy A., Lebedeva M.I. & Balashov V.N. (2023) How temperature-dependent silicate weathering acts as Earth's geological thermostat. *Science*, **379**, 382–389.

Bristow T.F., Kennedy M.J., Morrison K.D. & Mrofka D.D. (2012) The influence of authigenic clay formation on the mineralogy and stable isotopic record of lacustrine carbonates. *Geochimica et Cosmochimica Acta*, **90**, 64–82.

Buatier M., Früh-Green G. & Karpoff A. (1995) Mechanisms of Mg-phyllosilicate formation in a hydrothermal system at a sedimented ridge (Middle Valley, Juan de Fuca). *Contributions to Mineralogy and Petrology*, **122**, 134–151.

Cao C., Bataille C.P., Song H., Saltzman M.R., Cramer K.T., Wu H. *et al.* (2022) Persistent Late Permian to Early Triassic warmth linked to enhanced reverse weathering. *Nature Geoscience*, **15**, 832–838.

Caves J.K., Jost A.B., Lau K.V. & Maher K. (2016) Cenozoic carbon cycle imbalances and a variable weathering feedback. *Earth Planetary Science Letters*, **450**, 152–163.

Caves Rugenstein J.K. & Chamberlain C.P. (2018) The evolution of hydroclimate in Asia over the Cenozoic: a stable-isotope perspective. *Earth-Science Reviews*, **185**, 1129–1156.

Caves Rugenstein J.K., Ibarra D.E. & von Blanckenburg F. (2019) Neogene cooling driven by land surface reactivity rather than increased weathering fluxes. *Nature*, **571**, 99–102.

Cecil M.R. & Ducea M.N. (2011) K-Ca ages of authigenic sediments: examples from Paleozoic glauconite and applications to low-temperature thermochronometry. *International Journal of Earth Sciences*, **100**, 1783–1790.

Chanda P., Kohli A., Teng F.-Z. & Fantle M.S. (2023) Clay authigenesis in carbonate-rich sediments and its impact on carbonate diagenesis. *Geochimica et Cosmochimica Acta*, **346**, 76–101.

Charpentier D., Buatier M., Jacquot E., Gaudin A. & Wheat C.G. (2011) Conditions and mechanism for the formation of iron-rich montmorillonite in deep sea sediments (Costa Rica margin): coupling high-resolution mineralogical characterization and geochemical modeling. *Geochimica et Cosmochimica Acta*, **75**, 1397–1410.

Chen C., Lu A., Cai K. & Zhai Y. (2002) Sedimentary characteristics of Mg-rich carbonate formations and minerogenic fluids of magnesite and talc occurrences in early Proterozoic in eastern Liaoning Province, China. *Science in China Series B: Chemistry*, **45**, 84–92.

Chester R. (2000) *Marine Geochemistry*, 2nd edition. Blackwell Science, Hoboken, NJ, USA, 520 pp.

Clauer N., Keppens E. & Stille P. (1992) Sr isotopic constraints on the process of glauconitization. *Geology*, **20**, 133–136.

Clauer N., Williams L.B. & Fallick A.E. (2014) Genesis of nanometric illite crystals elucidated by light-element (hydrogen, lithium, boron and oxygen) isotope tracing, and K-Ar and Rb-Sr dating. *Chemical Geology*, **383**, 26–50.

Clauer N., Williams L.B. & Uysal I.T. (2022) Boron and lithium isotopic signatures of nanometer-sized smectite-rich mixed-layers of bentonite beds from Campos Basin (Brazil). *Clays and Clay Minerals*, **70**, 72–83.

Clauer N., Zwingmann H., Liewig N. & Wendling R. (2012) Comparative $^{40}Ar/^{39}Ar$ and K-Ar dating of illite-type clay minerals: a tentative explanation for age identities and differences. *Earth-Science Reviews*, **115**, 76–96.

Colbourn G., Ridgwell A. & Lenton T.M. (2015) The time scale of the silicate weathering negative feed-back on atmospheric CO_2. *Global Biogeochemical Cycles*, **29**, 583–596.

Conley D.J., Frings P.J., Fontorbe G., Clymans W., Stadmark J., Hendry K.R. *et al.* (2017) Biosilicification drives a decline of dissolved Si in the oceans through geologic time. *Frontiers in Marine Science*, **4**, 397.

Coogan L.A. & Dosso S.E. (2015) Alteration of ocean crust provides a strong temperature dependent feedback on the geological carbon cycle and is a primary driver of the Sr isotopic composition of seawater. *Earth and Planetary Science Letters*, **415**, 38–46.

Coogan L.A. & Gillis K.M. (2013) Evidence that low-temperature oceanic hydrothermal systems play an important role in the silicate-carbonate weathering cycle and long-term climate regulation. *Geochemistry, Geophysics, Geosystems*, **14**, 1771–1786.

Coogan L.A. & Gillis K.M. (2018) Low-temperature alteration of the seafloor: impacts on ocean chemistry. *Annual Review of Earth and Planetary Sciences*, **46**, 21–45.

Coogan L.A. & Gillis K.M. (2020) The average Phanerozoic CO_2 degassing flux estimated from the O-isotopic composition of seawater. *Earth and Planetary Science Letters*, **536**, 116151.

Craw D., Smith D.W. & Youngson J.H. (1995) Formation of authigenic Fe^{2+}-bearing smectite-vermiculite during terrestrial diagenesis, southern New Zealand. *New Zealand Journal of Geology and Geophysics*, **38**, 151–158.

Cuadros J. (2017) Clay minerals interaction with microorganisms: a review. *Clay Minerals*, **52**, 235–261.

Cuadros J., Andrade G., Ferreira T.O., de Moya Partiti C.S., Cohen R. & Vidal-Torrado P. (2017) The mangrove reactor: fast clay transformation and potassium sink. *Applied Clay Science*, **140**, 50–58.

Cuevas J., de la Villa R.V., Ramirez S., Petit S., Meunier A. & Leguey S. (2003) Chemistry of Mg smectites in lacustrine sediments from the Vicalvaro Sepiolite Deposit, Madrid Neogene Basin (Spain). *Clays and Clay Minerals*, **51**, 457–472.

Dale A.W., Geilert S., Diercks I., Fuhr M., Perner M., Scholz F. & Wallmann K. (2024) Seafloor alkalinity enhancement as a carbon dioxide removal strategy in the Baltic Sea. *Communications Earth and Environment*, **5**, 452.

Damyanov Z. & Vassileva M. (2001) Authigenic phyllosilicates in the Middle Triassic Kremikovtsi Sedimentary Exhalative Siderite Iron Formation, Western Balkan, Bulgaria. *Clays and Clay Minerals*, **49**, 559–585.

Davies N.S., Shillito A.P., Slater B.J., Liu A.G. & McMahon W.J. (2020) Evolutionary synchrony of Earth's biosphere and sedimentary–stratigraphic record. *Earth-Science Reviews*, **201**, 102979.

de Oliveira Nardi Leite C., de Assis Silva C.M. & de Ros L.F. (2020) Depositional and diagenetic processes in the pre-salt rift section of a Santos Basin area, SE Brazil. *Journal of Sedimentary Research*, **90**, 584–608.

Dekov V.M., Kamenov G.D., Stummeyer J., Thiry M., Savelli C., Shanks W.C. *et al.* (2007) Hydrothermal nontronite formation at Eolo Seamount (Aeolian volcanic arc, Tyrrhenian Sea). *Chemical Geology*, **245**, 103–119.

Derkowski A., Środoń J., Franus W., Uhlík P., Banaś M., Zieliński G. *et al.* (2009) Partial dissolution of glauconitic samples: implications for the methodology of K-Ar and Rb-Sr dating. *Clays and Clay Minerals*, **57**, 531–554.

Deyhle A. & Kopf A.J. (2005) The use and usefulness of boron isotopes in natural silicate–water systems. *Physics and Chemistry of the Earth, Parts A/B/C*, **30**, 1038–1046.

Duan Q., Jiang S., Chen F., Li Z., Ma L., Song Y. *et al.* (2023) Fabrication, evaluation methodologies and models of slow-release fertilizers: a review. *Industrial Crops and Products*, **192**, 1–22.

Dunlea A.G., Murray R.W., Santiago Ramos D.P. & Higgins J.A. (2017) Cenozoic global cooling and increased seawater Mg/Ca *via* reduced reverse weathering. *Nature Communications*, **8**, 844.

Dunn S.K., Pufahl P.K. & Lokier S.W. (2021) Middle Ordovician upwelling-related ironstone of north Wales: coated grains, ocean chemistry, and biological evolution. *Frontiers in Earth Sciences*, **9**, 669476.

Elderfield H. & Schultz A. (1996) Mid-ocean ridge hydrothermal fluxes and the chemical composition of the ocean. *Annual Review of Earth and Planetary Sciences*, **24**, 191–224.

Ehlert C., Doering K., Wallmann K., Scholz F., Sommer S., Grasse P. *et al.* (2016) Stable silicon isotope signatures of marine pore waters – biogenic opal dissolution versus authigenic clay mineral formation. *Geochimica et Cosmochimica Acta*, **191**, 102–117.

Eiler J.M. (2007) 'Clumped-isotope' geochemistry – the study of naturally-occurring, multiply-substituted isotopologues. *Earth and Planetary Science Letters*, **262**, 309–327.

Eriksson P.G., Martins-Neto M.A., Nelson D.R., Aspler L.B., Chiarenzelli J.R., Catuneanu O. *et al.* (2001) An introduction to Precambrian basins: their characteristics and genesis. *Sedimentary Geology*, **141**, 1–35.

Erkoyun H. & Kadir S. (2011) Mineralogy, micromorphology, geochemistry and genesis of a hydrothermal kaolinite deposit and altered Miocene host volcanites in the Hallaçlar area, Uşak, western Turkey. *Clay Minerals*, **46**, 421–448.

Fakhraee M., Li Z., Planavsky N.J. & Reinhard C.T. (2023) A biogeochemical model of mineral-based ocean alkalinity enhancement: impacts on the biological pump and ocean carbon uptake. *Environmental Research Letters*, **18**, 044047.

Farkaš J., Wallmann K., Mosley L., Staudigel P., Zheng X.-Y., Leyden E. *et al.* (2025) Alkalinity and elemental cycles in present and past ocean: insight from geochemical modeling and alkali and alkaline earth metal isotopes. Pp. 33–87 in: *Treatise on Geochemistry*, vol. 5, 3rd edition (A. Anbar & D. Weis, editors). Elsevier Science, Amsterdam, The Netherlands.

Feng E.Y., Koeve W., Keller D.P. & Oschlies A. (2017) Model-based assessment of the CO_2 sequestration potential of coastal ocean alkalinization. *Earth's Future*, **5**, 1252–1266.

Foster G.L. & Rohling E.J. (2013) Relationship between sea level and climate forcing by CO_2 on geological timescales. *Proceedings of the National Academy of Sciences of the United States of America*, **110**, 1209–1214.

Friedlingstein P., Houghton R.A., Marland G., Hackler J., Boden T.A., Conway T.J. *et al.* (2010) Update on CO_2 emissions. *Nature Geosciences*, **3**, 811–812.

Frings P. (2017) Revisiting the dissolution of biogenic Si in marine sediments: a key term in the ocean Si budget. *Acta Geochimica*, **36**, 429–432.

Fritz S.J. & Toth T.A. (1997) An Fe-berthierine from a Cretaceous laterite: part II. Estimation of Eh, pH and pCO_2 conditions of formation. *Clays and Clay Minerals*, **45**, 580–586.

Fu J., Wang C., Chen X., Huang Z. & Chen D. (2018) Classification research and types of slow controlled release fertilizers (SRFs) used – a review. *Communications in Soil Science and Plant Analysis*, **49**, 2219–2230.

Fuhr M., Geilert S., Schmidt M., Liebetrau V., Vogt C., Ledwig B. & Wallmann K. (2022) Kinetics of olivine weathering in seawater: an experimental study. *Frontiers in Climate*, 4, 831587.

Gaillardet J., Dupré B., Louvat P. & Allegre C. (1999) Global silicate weathering and CO_2 consumption rates deduced from the chemistry of large rivers. *Chemical Geology*, **159**, 3–30.

Galán E. (2006) Genesis of clay minerals. *Developments in Clay Science*, **1**, 1129–1162.

Galán E. & Pozo M. (2011) Palygorskite and sepiolite deposits in continental environments. Description, genetic patterns and sedimentary settings. *Developments in Clay Science*, **3**, 125–173.

Garrels R.M. (1965) Silica: role in the buffering of natural waters. *Science*, **148**, 69.

Garzanti E., Haas R. & Jadoul F. (1989) Ironstones in the Mesozoic passive margin sequence of the Tethys Himalaya (Zanskar, northern India): sedimentology and metamorphism. *Geological Society, London, Special Publications*, **46**, 229–244.

Geilert S., Frick D.A., Abbott A.N. & Löhr S.C. (2024) Marine clay maturation induces systematic silicon isotope decrease in authigenic clays and pore fluids. *Communications Earth and Environment*, **5**, 573.

Geilert S., Frick D.A., Garbe-Schönberg D., Scholz F., Sommer S., Grasse P. *et al.* (2023) Coastal El Niño triggers rapid marine silicate alteration on the seafloor. *Nature Communications*, **14**, 1676.

Ghosh R. (2020) Authigenic precipitation of ferric oxyhydroxides and greenalite in Archean oceans. *Chemical Geology*, **552**, 119777.

Gillis K.M. & Coogan L.A. (2011) Secular variation in carbon uptake into the ocean crust. *Earth and Planetary Science Letters*, **302**, 385–392.

Giresse P., Bayon G., Tallobre C. & Loncke L. (2021) Neodymium isotopes in glauconite for palaeoceanographic reconstructions at continental margins: a preliminary investigation from Demerara Rise. *Frontiers in Earth Sciences*, **9**, 652501.

Giresse P., Wiewióra A. & Grabska D. (2004) Glauconitization processes in the northwestern Mediterranean (Gulf of Lions). *Clay Minerals*, **39**, 57–73.

Gislason S.R., Oelkers E.H., Eiriksdottir E.S., Kardjilov M.I., Gisladottir G., Sigfusson B. *et al.* (2009) Direct evidence of the feedback between climate and weathering. *Earth and Planetary Science Letters*, **277**, 213–222.

Gorojovsky L. & Alard O. (2020) Optimisation of laser and mass spectrometer parameters for the in situ analysis of Rb/Sr ratios by LA-ICP-MS/MS. *Journal of Analytical Atomic Spectrometry*, **164**, 382–315.

Gough D. (1981) Solar interior structure and luminosity variations. *Solar Physics*, **74**, 21–34.

Grenne T. & Slack J.F. (2019) Mineralogy and geochemistry of silicate, sulfide, and oxide iron formations in Norway: evidence for fluctuating redox states of early Paleozoic marine basins. *Mineralium Deposita*, **54**, 829–848.

Gutierrez-Mas J.M., Lopez-Galindo A. & Lopez-Aguayo F. (1997) Clay minerals in recent sediments of the continental shelf and the Bay of Cádiz (SW Spain). *Clay Minerals*, **32**, 507–515.

Haley B.A., Du J., Abbott A.N. & McManus J. (2017) The impact of benthic processes on rare earth element and neodymium isotope distributions in the oceans. *Frontiers in Marine Science*, **4**, 858–812.

Han K., Han Z., Garzanti E., Zhu S., Yao H., Guo H. *et al.* (2023) Middle Jurassic ooidal ironstones (southern Tibet): formation processes and implications for the paleoceanography of eastern Neo-Tethys. *Frontiers in Earth Sciences*, **10**, 1055957.

Han S., Löhr S.C., Abbott A.N., Baldermann A., Farkaš J., McMahon W. *et al.* (2022a) Earth system science applications of next-generation SEM-EDS automated mineral mapping. *Frontier in Earth Sciences*, **10**, 956912.

Han S., Löhr S.C., Abbott A.N., Baldermann A., Shields G.A., Cui H. *et al.* (2024) Authigenic clay mineral constraints on spatiotemporal evolution of restricted, evaporitic conditions during deposition of the Ediacaran Doushantuo Formation. *Earth and Planetary Science Letters*, **626**, 118524.

Han S., Löhr S.C., Abbott A.N., Baldermann A., Voigt M. & Yu B. (2022b) Authigenic clay mineral evidence for restricted, evaporitic conditions during the emergence of the Ediacaran Doushantuo Biota. *Communications Earth and Environment*, **3**, 165.

Haq B. (2014) Cretaceous eustasy revisited. *Global and Planetary Change*, **113**, 44–58.

Hartmann J., Suitner N., Lim C., Schneider J., Marín-Samper L., Arístegui J. *et al.* (2023) Stability of alkalinity in ocean alkalinity enhancement (OAE) approaches – consequences for durability of CO_2 storage. *Biogeosciences*, **20**, 781–802.

Hazen R.M., Sverjensky D.A., Azzolini D., Bish D.L., Elmore S.C., Hinnov L. & Milliken R.E. (2013) Clay mineral evolution. *American Mineralogist*, **98**, 2007–2029.

He J. & Tyka M.D. (2023) Limits and CO_2 equilibration of near-coast alkalinity enhancement. *Biogeosciences*, **20**, 27–43.

Higgins J.A. & Schrag D.P. (2015) The Mg isotopic composition of Cenozoic seawater – evidence for a link between Mg-clays, seawater Mg/Ca, and climate. *Earth and Planetary Science Letters*, **416**, 73–81.

Hilley G.E. & Porder S. (2008) A framework for predicting global silicate weathering and CO_2 drawdown rates over geologic time-scales. *Proceedings of the National Academy of Sciences of the United States of America*, **105**, 16855–16859.

Hogmalm K.J., Zack T., Karlsson A.K.-O., Sjöqvist A.S.L. & Garbe-Schönberg D. (2017) In situ Rb-Sr and K-Ca dating by LA-ICP-MS/MS: an evaluation of N_2O and SF_6 as reaction gases. *Journal of Analytical Atomic Spectrometry*, **32**, 305–313.

Hornibrook E.R.C. & Longstaffe F.J. (1996) Berthierine from the Lower Cretaceous Clearwater Formation, Alberta, Canada. *Clays and Clay Minerals*, **44**, 1–21.

Hu Q., Yang B., Liu J., Li B., Dang Y., Zhu A. *et al.* (2023) Geochemical and mineral composition characteristics of hydrothermal-related clay-sized surface sediments from southern Mid-Atlantic Ridge: implications for hydrothermal depositional environment. *Ore Geology Reviews*, **162**, 105674.

Hu Y., Teng F.Z., Plank T. & Chauvel C. (2020) Potassium isotopic heterogeneity in subducting oceanic plates. *Science Advances*, **6**, eabb2472.

Huang K.-J., Teng F.-Z., Plank T., Staudigel H., Hu Y. & Bao Z.-Y. (2018) Magnesium isotopic composition of altered oceanic crust and the global Mg cycle. *Geochimica et Cosmochimica Acta*, **238**, 357–373.

Huang T., Shen B., Wang X., Ma H., Li C. & Zhou C. (2024) Extremely [26]Mg-enriched authigenic clays from the Ediacaran Doushantuo Formation (south China) indicating the coupled carbonate-silicate diagenesis. *Global and Planetary Change*, **239**, 104500.

Huang T.-H., Sun X., Somelar P., Kirsimäe K., Pickering R.A., Kim J.-H. *et al.* (2023) Separating Si phases from diagenetically-modified sediments through sequential leaching. *Chemical Geology*, **637**, 121681.

Huang T.-Y., Teng F.-Z., Rudnick R.L., Chen X.-Y., Hu Y., Liu Y.-S. & Wu F.-Y. (2020) Heterogeneous potassium isotopic composition of the upper continental crust. *Geochimica et Cosmochimica Acta*, **278**, 122–136.

Huggett J.M. & Cuadros J. (2010) Glauconite formation in lacustrine/palaeosol sediments, Isle of Wight (Hampshire Basin), UK. *Clay Minerals*, **45**, 35–49.

Iglesias-Rodríguez M.D., Rickaby R.E.M., Singh A. & Gately J.A. (2023) Laboratory experiments in ocean alkalinity enhancement research. *State of the Planet*, **5**, 1–18.

Iijima A. & Matsumoto R. (1982) Berthierine and chamosite in coal measures of Japan. *Clays and Clay Minerals*, **30**, 264–274.

Isphording W.C. (1973) Discussion of the occurrence and origin of sedimentary palygorskite-sepiolite deposits. *Clays and Clay Minerals*, **21**, 391–401.

Isson T.T. & Planavsky N.J. (2018) Reverse weathering as a long-term stabilizer of marine pH and planetary climate. *Nature*, **560**, 471.

Isson T. & Rauzi S. (2024) Oxygen isotope ensemble reveals Earth's seawater, temperature, and carbon cycle history. *Science*, **383**, 666–670.

Isson T.T., Planavsky N.J., Coogan L.A., Stewart E.M., Ague J.J., Bolton E.W. *et al.* (2020) Evolution of the global carbon cycle and climate regulation on Earth. *Global Biogeochemical Cycles*, **34**, e2018GB006061.

Jeans C.V. (2006) Clay mineralogy of the Cretaceous strata of the British Isles. *Clay Minerals*, **41**, 47–150.

Jin H., Wan S., Liu C., Zhao D., Pei W., Yu Z. *et al.* (2023) Evolution of silicate weathering in south China since 30 Ma: controlling factors and global implications. *Global and Planetary Change*, **223**, 104095.

Johnson J.E., Muhling J.R., Cosmidis J., Rasmussen B. & Templeton A.S. (2018) Low-Fe(III) greenalite was a primary mineral from Neoarchean oceans. *Geophysical Research Letters*, **45**, 3182–3192.

Jourdan F., Féraud G., Bertrand H., Kampunzu A.B., Tshoso G., Watkeys M.K. & Le Gall B. (2005) Karoo large igneous province: brevity, origin, and relation to mass extinction questioned by new $^{40}Ar/^{39}Ar$ age data. *Geology*, **33**, 745–748.

Kadir S., Erman H. & Erkoyun H. (2011) Mineralogical and geochemical characteristics and genesis of hydrothermal kaolinite deposits within Neogene volcanites, Kütahya (western Anatolia), Turkey. *Clays and Clay Minerals*, **59**, 250–276.

Kalderon-Asal B., Katchinoff J.A.R., Planavsky N.J., Hood A.v.S., Dellinger M., Bellefroid E.J. *et al.* (2021) A lithium-isotope perspective on the evolution of carbon and silicon cycles. *Nature*, **595**, 394–398.

Kalinina N., Maximov P., Molukpayeva D., Sherstyukov M., Kerimov A.-G. & Rudmin M. (2024) Depositional palaeoenvironment of the Middle Jurassic (Aalenian) ooidal

ironstones in Labino-Malkin zone (north-western Caucasus). *Marine and Petroleum Geology*, **162**, 106744.

Kasting J.F. (2019) The Goldilocks planet? How silicate weathering maintains Earth 'just right'. *Elements*, **15**, 235–240.

Keller C. & Wood B. (1993) Possibility of chemical weathering before the advent of vascular land plants. *Nature*, **364**, 223–225.

Kelley S. (2002) Excess argon in K-Ar and Ar-Ar geochronology. *Chemical Geology*, **188**, 1–22.

Kennedy M., Droser M., Mayer L.M., Pevear D. & Mrofka D. (2006) Late Precambrian oxygenation; inception of the clay mineral factory. *Science*, **311**, 1446–1449.

Klein C. (2005) Some Precambrian banded iron-formations (BIFs) from around the world: their age, geologic setting, mineralogy, metamorphism, geochemistry, and origins. *American Mineralogist*, **90**, 1473–1499.

Kloprogge J.T. (1998) Synthesis of smectites and porous pillared clay catalysts: a review. *Journal of Porous Materials*, **5**, 5–41.

Köhler B., Singer A. & Stoffers P. (1994) Biogenic nontronite from marine white smoker chimneys. *Clays and Clay Minerals*, **42**, 681–701.

Köhler P., Abrams J.F., Völker C., Hauck J. & Wolf-Gladrow D.A. (2013) Geoengineering impact of open ocean dissolution of olivine on atmospheric CO_2, surface ocean pH and marine biology. *Environmental Research Letters*, **8**, 014009.

Konhauser K.O. & Urrutia M.M. (1999) Bacterial clay authigenesis: a common biogeochemical process. *Chemical Geology*, **161**, 399–413.

Konhauser K.O., Planavsky N.J., Hardisty D.S., Robbins L.J., Warchola T.J., Haugaard R. *et al.* (2017) Iron formations: a global record of Neoarchaean to Palaeoproterozoic environmental history. *Earth-Science Reviews*, **172**, 140–177.

Köster H., Williams L.B., Kudejova P. & Gilg H.A. (2019) The boron isotope geochemistry of smectites from sodium, magnesium and calcium bentonite deposits. *Chemical Geology*, **510**, 166–187.

Krissansen-Totton J. & Catling D.C. (2020) A coupled carbon-silicon cycle model over Earth history: reverse weathering as a possible explanation of a warm mid-Proterozoic climate. *Earth and Planetary Science Letters*, **537**, 116181.

Kump L.R. & Arthur M.A. (1997) Global chemical erosion during the Cenozoic: weatherability balances the budgets. Pp. 399–426 in: *Tectonic Uplift and Climate Change* (W.F. Ruddiman, editor). Plenum Press, New York, NY, USA.

Kump L.R., Brantley S.L. & Arthur M.A. (2000) Chemical weathering, atmospheric CO_2, and climate. *Annual Review of Earth and Planetary Sciences*, **28**, 611–667.

Laureijs C.T., Coogan L.A. & Spence J. (2021a) *In-situ* Rb-Sr dating of celadonite from altered upper oceanic crust using laser ablation ICP-MS/MS. *Chemical Geology*, **579**, 120339.

Laureijs C.T., Coogan L.A. & Spence J. (2021b) Regionally variable timing and duration of celadonite formation in the Troodos lavas (Cyprus) from Rb-Sr age distributions. *Chemical Geology*, **560**, 119995.

Lei Z., Cagnetta G., Li X., Qu J., Li Z., Zhang Q. & Huang J. (2018) Enhanced adsorption of potassium nitrate with potassium cation on H_3PO_4 modified kaolinite and nitrate anion into Mg-Al layered double hydroxide. *Applied Clay Science*, **154**, 10–16.

Lempart-Drozd M., Blachowski A., Gumsley A. & Ciesielska, Z. (2022) Thermal decomposition of minnesotaite and dehydrogenation during Fe^{2+} oxidation, with implications for redox reactions in banded iron formations. *Chemical Geology*, **601**, 120867.

Lenton T.M., Crouch M., Johnson M., Pires N. & Dolan L. (2012) First plants cooled the Ordovician. *Nature Geoscience*, **5**, 86–89.

Li F., Penman D., Planavsky N., Knudsen A., Zhao M., Wang X. *et al.* (2021a) Reverse weathering may amplify post-Snowball atmospheric carbon dioxide levels. *Precambrian Research*, **364**, 106279.

Li F., Zhang P., Ma X. & Yuan G. (2021b) The iron oolitic deposits of the lower Devonian Yangmaba formation in the Longmenshan area, Sichuan Basin. *Marine and Petroleum Geology*, **130**, 105137.

Li G.L., Zhou C.H., Fiore S. & Yu W.H. (2019a) Interactions between microorganisms and clay minerals: new insights and broader applications. *Applied Clay Science*, **177**, 91–113.

Li S., Li W., Beard B.L., Raymo M.E., Wang X., Chen Y. & Chen J. (2019b) K isotopes as a tracer for continental weathering and geological K cycling. *Proceedings of the National Academy of Sciences of the United States of America*, **116**, 8740–8745.

Li W., Li S. & Beard B.L. (2019c) Geological cycling of potassium and the K isotopic response: insights from loess and shales. *Acta Geochimica*, **38**, 508–516.

Li W., Liu X.-M., Hu Y., Teng F.-Z. & Hu Y. (2021c) Potassium isotopic fractionation during clay adsorption. *Geochimica et Cosmochimica Acta*, **304**, 160–177.

Li W., Liu X.-M., Wang K., McManus J., Haley B.A., Takahashi Y. *et al.* (2022a) Potassium isotope signatures in modern marine sediments: insights into early diagenesis. *Earth and Planetary Science Letters*, **599**, 117849.

Li W., Liu X.-M., Wang K., Hu Y., Suzuki A. & Yoshimura T. (2022b) Potassium incorporation and isotope fractionation in cultured scleractinian corals. *Earth and Planetary Science Letters*, **581**, 117393.

Lima B.E.M. & De Ros L.F. (2019) Deposition, diagenetic and hydrothermal processes in the Aptian Pre-Salt lacustrine carbonate reservoirs of the northern Campos Basin, offshore Brazil. *Sedimentary Geology*, **383**, 55–81.

Linnemann U., Ovtcharova M., Schaltegger U., Gärtner A., Hautmann M., Geyer G. *et al.* (2018) New high-resolution age data from the Ediacaran–Cambrian boundary indicate rapid, ecologically driven onset of the Cambrian explosion. *Terra Nova*, **31**, 49–58.

Lipp A.G., Shorttle O., Sperling E.A., Brocks J.J., Cole D.B., Crockford P.W. *et al.* (2021) The composition and weathering of the continents over geologic time. *Geochemical Perspectives Letters*, **17**, 21–26.

Liu W., Price S., Bennett G., Maxwell T.M.R., Zhao C., Walker G. & Bunt C. (2022) A landscape review of controlled release urea products: patent objective, formulation and technology. *Journal of Controlled Release*, **348**, 612–630.

Logvinenko N.V. (1982) Origin of glauconite in the recent bottom sediments of the ocean. *Sedimentary Geology*, **31**, 43–48.

López-Quirós A., Escutia C., Sánchez-Navas A., Nieto F., Garcia-Casco A., Martín-Algarra A. *et al.* (2019) Glaucony authigenesis, maturity and alteration in the Weddell Sea: an indicator of paleoenvironmental conditions before the onset of Antarctic glaciation. *Scientific Reports*, **9**, 13580.

López-Quirós A., Lobo F.J., Mendes I. & Nieto, F. (2023) Holocene glaucony from the Guadiana Shelf, northern Gulf of Cadiz (SW Iberia): new genetic insights in a sequence stratigraphy context. *Minerals*, **13**, 177.

Loucaides S., Michalopoulos P., Presti M., Koning E., Behrends T. & Van Cappellen P. (2010) Seawater-mediated interactions between diatomaceous silica and terrigenous sediments: results from long-term incubation experiments. *Chemical Geology*, **270**, 68–79.

Ma J., Shi X., Lechte M., Zhou X., Wang Z., Huang K. *et al.* (2022) Mesoproterozoic seafloor authigenic glauconite-berthierine: indicator of enhanced reverse weathering on early Earth. *American Mineralogist*, **107**, 116–130.

Mackenzie F.T. & Garrels R.M. (1966a) Chemical mass balance between rivers and oceans. *American Journal of Science*, **264**, 507–525.

Mackenzie F.T. & Garrels R.M. (1966b) Silica-bicarbonate balance in the ocean and early diagenesis. *Journal of Sedimentary Research*, **36**, 1075–1084.

Mackenzie F.T. & Kump L.R. (1995) Reverse weathering, clay mineral formation, and oceanic element cycles. *Science*, **270**, 5236.

Mackin J.E. & Aller R.C. (1984) Dissolved Al in sediments and waters of the East China Sea: implications for authigenic mineral formation. *Geochimica et Cosmochimica Acta*, **48**, 281–297.

Maher K. & Chamberlain C.P. (2014) Hydrologic regulation of chemical weathering and the geologic carbon cycle. *Science*, **343**, 6178.

Maliva R.G., Dickson J.A.D. & Fallick A.E. (1999) Kaolin cements in limestones; potential indicators of organic-rich pore waters during diagenesis. *Journal of Sedimentary Research*, **69**, 158–163.

Mandal S., Banerjee S., Sarkar S., Mondal I. & Roy Choudhury T. (2020) Origin and sequence stratigraphic implications of high-alumina glauconite within the Lower Quartzite, Vindhyan Supergroup. *Marine and Petroleum Geology*, **112**, 104040.

Mandal S., Roy Choudhury T., Das A., Sarkar S. & Banerjee S. (2022) Shallow marine glauconitization during the Proterozoic in response to intrabasinal tectonics: a study from the Proterozoic Lower Bhander Sandstone, central India. *Precambrian Research*, **372**, 106596.

Marín-Samper L., Arístegui J., Hernández-Hernández N., Ortiz J., Archer S.D., Ludwig A. & Riebsell U. (2024) Assessing the impact of CO_2-equilibrated ocean alkalinity enhancement on microbial metabolic rates in an oligotrophic system. *Biogeosciences*, **21**, 2859–2876.

Maring H.B. & Duce R.A. (1987) The impact of atmospheric aerosols on trace metal chemistry in open ocean surface seawater, 1. Aluminum. *Earth and Planetary Science Letters*, **84**, 381–392.

Maximov P., Dasi E., Kalinina N., Ruban A., Pokidko B. & Rudmin M. (2023) Zinc-intercalated halloysite nanotubes as potential nanocomposite fertilizers with targeted delivery of micronutrients. *Materials*, **16**, 6729.

Maynard J.B. (1986) Geochemistry of oolitic iron ores, an electron microprobe study. *Economic Geology*, **81**, 1473–1483.

McMahon W.J. & Davies N.S. (2018) Evolution of alluvial mudrock forced by early land plants. *Science*, **359**, 1022–1024.

Meier F., Rickels W., Quaas M. & Traeger C. (2022) Carbon dioxide removal in a global analytic climate economy. *Kiel Working Paper*, **2227**, 1–29.

Meunier A. & El Albani A. (2007) The glauconite–Fe-illite–Fe-smectite problem: a critical review. *Terra Nova*, **19**, 95–104.

Meysman F.J.R. & Montserrat F. (2017) Negative CO_2 emissions *via* enhanced silicate weathering in coastal environments. *Biology Letters*, **13**, 20160905.

Michalopoulos P. & Aller R.C. (1995) Rapid clay mineral formation in Amazon delta sediments: reverse weathering and oceanic elemental cycles. *Science*, **270**, 614–617.

Michalopoulos P. & Aller R.C. (2004) Early diagenesis of biogenic silica in the Amazon delta: alteration, authigenic clay formation, and storage. *Geochimica et Cosmochimica Acta*, **68**, 1061–1085.

Michalopoulos P., Aller R.C. & Reeder R.J. (2000) Conversion of diatoms to clays during early diagenesis in tropical, continental shelf muds. *Geology*, **28**, 1095–1098.

Millikin A.E.G., Strauss J.V., Halverson G.P., Bergmann K.D., Tosca N.J. & Rooney A.D. (2022) Calibrating the Russøya excursion in Svalbard, Norway, and implications for Neoproterozoic chronology. *Geology*, **50**, 506–510.

Misra S. & Froehlich P.N. (2012) Lithium isotope history of Cenozoic seawater: changes in silicate weathering and reverse weathering. *Science*, **335**, 818–823.

Mohanty S.P. & Mishra P.K. (2023) Greenalite-chamosite composition, geothermometry and oxygen fugacity variations in pisolitic ironstone and carbonates of the Chilpi Group: implication on Paleoproterozoic seawater chemistry. *Physics and Chemistry of Minerals*, **50**, 34.

Montserrat F., Renforth P., Hartmann J., Leermakers M., Knops P. & Meysman F.J.R. (2017) Olivine dissolution in seawater: implications CO_2 sequestration through enhanced weathering in coastal environments. *Environmental Science and Technology*, **51**, 3960–3972.

Moradi S., Babapoor A., Ghanbarlou S., Kalashgarani M.Y., Salahshoori I. & Seyfaee A. (2023) Toward a new generation of fertilizers with the approach of controlled-release fertilizers: a review. *Journal of Coatings Technology and Research*, **21**, 31–54.

Morris R. (1993) Genetic modelling for banded iron-formation of the Hamersley Group, Pilbara Craton, Western Australia. *Precambrian Research*, **60**, 243–286.

Morrow D.R., Thompson M.S., Anderson A., Batres M., Buck H.J., Dooley K. *et al.* (2020) Principles for thinking about carbon dioxide removal in just climate policy. *One Earth*, **3**, 150–153.

Mücke A. (2006) Chamosite, siderite and the environmental conditions of their formation in chamosite-type Phanerozoic ooidal ironstones. *Ore Geology Reviews*, **28**, 235–249.

Muhling J.R. & Rasmussen B. (2020) Widespread deposition of greenalite to form banded iron formations before the Great Oxidation Event. *Precambrian Research*, **339**, 105619.

Müller R.D., Dutkiewicz A., Seton M. & Gaina C. (2013) Seawater chemistry driven by supercontinent assembly, breakup, and dispersal. *Geology*, **41**, 907–910.

Müller R.D., Mather B., Dutkiewicz A., Keller T., Merdith A., Gonzalez C.M. *et al.* (2022) Evolution of Earth's tectonic carbon conveyor belt. *Nature*, **605**, 629–639.

Netto P.R.A., Pozo M., da Silva M.D., Mexias A.S., Gomes M.E.B., Borghi L. & Rios-Netto A.M. (2022) Authigenic Mg-clay assemblages in the Barra Velha Formation (Upper Cretaceous) from Santos Basin (Brazil): the role of syngenetic and diagenetic process. *Applied Clay Science*, **216**, 106339.

Noack Y., Decarreau A., Boudzoumou F. & Trompette R. (1989) Low-temperature oolitic talc in Upper Proterozoic rocks, Congo. *Journal of Sedimentary Petrology*, **59**, 717–723.

Oelkers E.H., Benning L.G., Lutz S., Mavromatis V., Pearce C.R. & Plümper O. (2015) The efficient long-term inhibition of forsterite dissolution by common soil bacteria and fungi at Earth surface conditions. *Geochimica et Cosmochimica Acta*, **168**, 222–235.

Pe-Piper G., Dolansky L. & Piper D.J.W. (2005) Sedimentary environment and diagenesis of the Lower Cretaceous Chaswood Formation, southeastern Canada: the origin of kaolin-rich mudstones. *Sedimentary Geology*, **178**, 75–97.

Penman D.E., Rugenstein J.K.C., Ibarra D.E. & Winnick M.J. (2020) Silicate weathering as a feedback and forcing in Earth's climate and carbon cycle. *Earth-Science Reviews*, **209**, 103298.

Pereira E.I., da Cruz C.C.T., Solomon A., Le A., Cavigelli M.A. & Ribeiro C. (2015) Novel slow-release nanocomposite nitrogen fertilizers: the impact of polymers on nanocomposite properties and function. *Industrial & Engineering Chemistry Research*, **54**, 3717–3725.

Pestitschek B., Gier S., Essa M. & Kurzweil H. (2012) Effects of weathering on glauconite: evidence from the Abu Tartur Plateau, Egypt. *Clays and Clay Minerals*, **60**, 76–88.

Pickard A.L. (2003) SHRIMP U–Pb zircon ages for the Palaeoproterozoic Kuruman Iron Formation, Northern Cape Province, South Africa: evidence for simultaneous BIF deposition on Kaapvaal and Pilbara Cratons. *Precambrian Research*, **125**, 275–315.

Pickering R.A., Cassarino L., Hendry K.R., Wang X.L., Maiti K. & Krause J.W. (2020) Using stable isotopes to disentangle marine sedimentary signals in reactive silicon pools. *Geophysical Research Letters*, **47**, 1–11.

Pogge von Strandmann P.A.E., Burton K.W., James R.H., van Calsteren P., Gislason S.R. & Sigfusson B. (2008) The influence of weathering processes on riverine magnesium isotopes in a basaltic terrain. *Earth and Planetary Science Letters*, **276**, 187–197.

Pogge von Strandmann P.A.E., Jenkyns H.C. & Woodfine R.G. (2013) Lithium isotope evidence for enhanced weathering during Oceanic Anoxic Event 2. *Nature Geoscience*, **6**, 668–672.

Porada P., Lenton T.M., Pohl A., Weber B., Mander L., Donnadieu Y. *et al.* (2016) High potential for weathering and climate effects of non-vascular vegetation in the Late Ordovician. *Nature Communications*, **7**, 12113.

Post J.L. (1984) Saponite from near Ballarat, California. *Clays and Clay Minerals*, **32**, 147–153.

Post J.L., Cupp B.L. & Madsen F.T. (1997) Beidellite and associated clays from the DeLamar Mine and Florida Mountain Area, Idaho. *Clays and Clay Minerals*, **45**, 240–250.

Poulton S.W. & Canfield D.E. (2011) Ferruginous conditions: a dominant feature of the ocean through Earth's history. *Elements*, **7**, 107–112.

Pozo M. & Calvo J.P. (2018) An overview of authigenic magnesian clays. *Minerals*, **8**, 520.

Presti M. & Michalopoulos P. (2008) Estimating the contribution of the authigenic mineral component to the long-term reactive silica accumulation on the western shelf of the Mississippi River Delta. *Continental Shelf Research*, **28**, 823–838.

Rafiei M., Löhr S., Alard O., Baldermann A., Farkaš J. & Brock G.A. (2023) Microscale petrographic, trace element, and isotopic constraints on glauconite diagenesis in altered sedimentary sequences: implications for glauconite geochronology. *Geochemistry, Geophysics, Geosystems*, **24**, e2022GC010795.

Rafiei M., Löhr S., Baldermann A., Webster R. & Kong C. (2020) Quantitative petrographic differentiation of detrital *vs* diagenetic clay minerals in marine sedimentary sequences: implications for the rise of biotic soils. *Precambrian Research*, **350**, 105948.

Rahman S. & Trower E.J. (2023) Probing surface Earth reactive silica cycling using stable Si isotopes: mass balance, fluxes, and deep time implications. *Science Advances*, **9**, eadi2440.Rahman S., Aller R.C. & Cochran J.K. (2016) Cosmogenic ^{32}Si as a tracer of

biogenic silica burial and diagenesis: major deltaic sinks in the silica cycle. *Geophysical Research Letters*, **43**, 7124–7132.

Rahman S., Aller R.C. & Cochran J.K. (2017) The missing silica sink: revisiting the marine sedimentary Si cycle using cosmogenic ^{32}Si. *Global Biogeochemical Cycles*, **31**, 1559–1578.

Rahman M.H., Haque K.M.S. & Khan M.Z.H. (2021) A review on application of controlled released fertilizers influencing the sustainable agricultural production: a cleaner production process. *Environmental Technology & Innovation*, **23**, 101697.

Raiswell R. (2006) Towards a global highly reactive iron cycle. *Journal of Geochemical Exploration*, **88**, 436–439.

Raiswell R. & Canfield D.E. (2012) The iron biogeochemical cycle past and present. *Geochemical Perspectives*, **1**, 1–222.

Rasmussen B., Meier D.B., Krapež B. & Muhling J.R. (2013) Iron silicate microgranules as precursor sediments to 2.5-billion-year-old banded iron formations. *Geology*, **41**, 435–438.

Rasmussen B., Muhling J.R. & Krapež, B. (2021) Greenalite and its role in the genesis of early Precambrian iron formations – a review. *Earth-Science Reviews*, **217**, 103613.

Rasmussen B., Muhling J.R., Suvorova A. & Krapež B. (2017) Greenalite precipitation linked to the deposition of banded iron formations downslope from a late Archean carbonate platform. *Precambrian Research*, **290**, 49–62.

Rasmussen M.G., Bay E., Co M. & Road F.H. (1998) Low temperature fayalite, greenalite, and minnesotaite from the overlook gold deposit, Washington: phase relations in the system FeO–SiO$_2$–H$_2$O. *The Canadian Mineralogist*, **36**, 147–162.

Rauzi S., Foster W.J., Takahashi S., Hon R.S., Beaty B.J., Tarhan L.G. & Isson T. (2024) Lithium isotopic evidence for enhanced reverse weathering during the Early Triassic warm period. *Proceedings of the National Academy of Sciences of the United States of America*, **121**, e2318860121.

Raymo M.E. & Ruddiman W.F. (1992) Tectonic forcing of late Cenozoic climate. *Nature*, **359**, 117–122.

Redaa A., Farkaš J., Gilbert S., Collins A.S., Löhr S., Vasegh D. *et al.* (2023) Testing nano-powder and fused-glass mineral reference materials for *in situ* Rb-St dating of glauconite, phlogipite, biotite and feldspar *via* LA-ICP-MS/MS. *Geostandards and Geoanalytical Research*, **47**, 23–48.

Ren M., Zhao P., Cui X., Wang C., Zhang Y., Guo L. *et al.* (2024) Enhanced fertilizer utilization and heavy metals immobilization by ball-milling bentonite with NH_4Cl: experiments and DFT calculations. *Journal of Hazardous Materials*, **466**, 133616.

Richoz S., Baldermann A., Frauwallner A., Harzhauser M., Daxner-Höck G., Klammer D. & Piller W.E. (2017) Geochemistry and mineralogy of the Oligo-Miocene sediments of the Valley of Lakes, Mongolia. *Palaeobiodiversity and Palaeoenvironments*, **97**, 233–258.

Rooney A.D., Strauss J.V., Brandon A.D. & Macdonald F.A. (2015) A Cryogenian chronology: two long-lasting synchronous Neoproterozoic glaciations. *Geology*, **43**, 459–462.

Roy Choudhury T., Khanolkar S. & Banerjee S. (2022) Glauconite authigenesis during the warm climatic events of Paleogene: case studies from shallow marine sections of western India. *Global and Planetary Change*, **214**, 103857.

Roy Choudhury T., Srimani S., Mondal I., Chakrabarty A., Banerjee S. & Sarkar S. (2024) Berthierine authigenesis as grain pseudomorph? A new insight from the early Maastrichtian Kallankurichchi Formation, India. *Applied Clay Science*, **249**, 107255.

Royer D.L., Berner R.A., Montañez I.P., Tabor N.J. & Beerling D.J. (2004) CO_2 as a primary driver of Phanerozoic climate. *The Geological Society of America Today*, **14**, 4–10.

Rubio B. & López-Pérez A.E. (2024) Exploring the genesis of glaucony and verdine facies for paleoenvironmental interpretation: a review. *Sedimentary Geology*, **461**, 106579.

Rudmin M., Banerjee S., Maximov P., Novoselov A., Trubin Y., Smirnov P. *et al.* (2022a) Origin of ooids, peloids and micro-oncoids of marine ironstone deposits in Western Siberia (Russia). *Journal of Asian Earth Sciences*, **237**, 105361.

Rudmin M., Banerjee S. & Mazurov A. (2017) Compositional variation of glauconites in Upper Cretaceous–Paleogene sedimentary iron-ore deposits in south-eastern Western Siberia. *Sedimentary Geology*, **355**, 20–30.

Rudmin M., Banerjee S., Sinkina E., Ruban A., Kalinina N. & Smirnov P. (2022b) A study of iron carbonates and clay minerals for understanding the origin of marine ooidal ironstone deposits. *Marine and Petroleum Geology*, **142**, 105777.

Rudmin M., Kalinina N., Banerjee S., Reva I., Kondrashova E., Kanaki A. *et al.* (2021) Origin of Oligocene channel ironstones of Lisakovsk deposit (Turgay depression, northern Kazakhstan). *Ore Geology Reviews*, **138**, 104391.

Rudmin M., López-Quirós A., Banerjee S., Ruban A., Shaldybin M., Bernatonis P. *et al.* (2023a) Origin of Fe-rich clay minerals in Early Devonian volcanic rocks of the northern Minusa basin, Eastern Siberia. *Applied Clay Science*, **241**, 107014.

Rudmin M., Makarov B., López-Quirós A., Maximov P., Lokteva V., Ibraeva K. *et al.* (2023b) Preparation, features, and efficiency of nanocomposite fertilisers based on glauconite and ammonium dihydrogen phosphate. *Materials*, **16**, 6080.

Rudmin M., Mazurov A. & Banerjee S. (2019) Origin of ooidal ironstones in relation to warming events: Cretaceous–Eocene Bakchar deposit, south-east Western Siberia. *Marine and Petroleum Geology*, **100**, 309–325.

Sánchez-Roa C., Jiménez-Millán J., Abad I., Faulkner D.R., Nieto F. & García-Tortosa F.J. (2016) Fibrous clay mineral authigenesis induced by fluid-rock interaction in the Galera fault zone (Betic Cordillera, SE Spain) and its influence on fault gouge frictional properties. *Applied Clay Science*, **134**, 275–288.

Santiago Ramos D.P., Coogan L.A., Murphy J.G. & Higgins J.A. (2020) Low-temperature oceanic crust alteration and the isotopic budgets of potassium and magnesium in seawater. *Earth and Planetary Science Letters*, **541**, 116290.

Savin S.M. & Epstein, S. (1970) The oxygen and hydrogen isotope geochemistry of clay minerals. *Geochimica et Cosmochimica Acta*, **34**, 25–42.

Savko K.A. (2006) Phase equilibria in rocks of the Paleoproterozoic banded iron formation (BIF) of the Lebedinskoe deposit, Kursk Magnetic Anomaly, and the petrogenesis of BIF with alkali amphiboles. *Petrology*, **14**, 567–587.

Scheiblhofer E., Moser U., Löhr S., Wilmsen M., Farkaš J., Gallhofer D. *et al.* (2022) Revisiting glauconite geochronology: lessons learned from *in situ* radiometric dating of a glauconite-rich Cretaceous Shelfal Sequence. *Minerals*, **12**, 818.

Schieber J., Sur S. & Banerjee S. (2007) Benthic microbial mats in black shale units from the Vindhyan Supergroup, Middle Proterozoic of India: the challenges of recognizing the genuine article. Pp. 189–197 in: *Atlas of Microbial Mat Features Preserved within the*

Clastic Rock Record (J. Schieber, P.K. Bose, P.G. Eriksson, S. Banerjee, S. Sarkar, W. Altermann & O. Catuneau, editors). Elsevier, Amsterdam, The Netherlands.

Schön W., Mittermayr F., Leis A., Mischak I. & Dietzel M. (2016) Temporal and spatial variability of chemical and isotopic composition of soil solutions from cambisols – field study and experiments. *Science of the Total Environment*, **572**, 1066–1079.

Schott J., Mavromatis V., Fujii T., Pearce C.R. & Oelkers E.H. (2016) The control of carbonate mineral Mg isotope composition by aqueous speciation: theoretical and experimental modeling. *Chemical Geology*, **445**, 120–134.

Schott J., Pokrovsky O.S., Spalla O., Devreux F., Gloter A. & Mielczarski J.A. (2012) Formation, growth and transformation of leached layers during silicate minerals dissolution: the example of wollastonite. *Geochimica et Cosmochimica Acta*, **98**, 259–281.

Šegvić B., Zanoni G. & Moscariello A. (2020) On the origins of eogenetic chlorite in verdine facies sedimentary rocks from the Gabon Basin in West Africa. *Marine and Petroleum Geology*, **112**, 104064.

Selby D. (2009) U-Pb zircon geochronology of the Aptian/Albian boundary implies that the GL-O international glauconite standard is anomalously young. *Cretaceous Research*, **30**, 1263–1267.

Setti M., Marinoni L. & López-Galindo A. (2004) Mineralogical and geochemical characteristics (major, minor, trace elements and *REE*) of detrital and authigenic clay minerals in a Cenozoic sequence from Ross Sea, Antarctica. *Clay Minerals*, **39**, 405–421.

Sharma G.C. (1979) Controlled-release fertilizers and horticultural applications. *Scientia Horticulturae*, **11**, 107–129.

Sheldon N.D., Mitchell R.L. & Dzombak R.M. (2021) *Reconstructing Precambrian pCO₂ and pO₂ Using Paleosols*. Cambridge University Press, Cambridge, UK, 75 pp.

Siever R. (1992) The silica cycle in the Precambrian. *Geochimica et Cosmochimica Acta*, **56**, 3265–3272.

Simon M., Grossart H.P., Schweitzer B. & Ploug H. (2002) Microbial ecology of organic aggregates in aquatic ecosystems. *Aquatic Microbial Ecology*, **28**, 175–211.

Singer A. (1980) The paleoclimatic interpretation of clay minerals in soils and weathering profiles. *Earth Science Reviews*, **15**, 303–326.

Singer A. (1984) The paleoclimatic interpretation of clay minerals in sediments – a review. *Earth Science Reviews*, **21**, 251–293.

Singh P., Banerjee S., Pande K., Bhattacharya S., Sarkar S. & Le Pera E. (2022) Authigenic green mica in interflow horizons within Late Cretaceous Deccan Volcanic Province, India and its genetic implications. *Minerals*, **12**, 198.

Singh P., Banerjee S., Roy Choudhury T., Bhattacharya S. & Pande K. (2023) Distinguishing celadonite from glauconite for environmental interpretations: a review. *Journal of Palaeogeography*, **12**, 179–194.

Smith P.E., Evenson N.M., York D. & Odin G.S. (1998) Single-grain ^{40}Ar-^{39}Ar ages of glauconies: implications for the geologic time scale and global sea level variations. *Science*, **279**, 1517–1519.

Środoń J., Williams L., Szcerba M., Zaitseva T., Bojanowski M.J., Marciniak-Maliszewska B. *et al.* (2023) Mechanism of late diagenetic alteration of glauconite and implications for geochronology. *Geochimica et Cosmochimica Acta*, **352**, 157–174.

Steiner Z., Rae J.W.B., Berelson W.M., Adkins J.F., Hou Y., Dong S. *et al.* (2022) Authigenic formation of clay minerals in the abyssal North Pacific. *Global Biogeochemical Cycles*, **36**, e2021GB007270.

Stoch L. & Sikora W. (1976) Transformations of micas in the process of kaolinitization of granites and gneisses. *Clays and Clay Minerals*, **24**, 156–162.

Subarkah D., Blades M.L., Collins A.S., Farkaš J., Gilbert S., Löhr S.C. *et al.* (2022) Unraveling the histories of Proterozoic shales through in situ Rb-Sr dating and trace element laser ablation analysis. *Geology*, **50**, 66–70.

Subarkah D., Nixon A.L., Gilbert S.E., Collins A.S., Blades M.L., Simpson A. *et al.* (2024) Double dating sedimentary sequences using new applications of *in-situ* laser ablation analysis. *Lithos*, **480–481**, 107649.

Sun X. & Turchyn A.V. (2014) Significant contribution of authigenic carbonate to marine carbon burial. *Nature Geoscience*, **7**, 201–204.

Sun X., Higgins J. & Turchyn A.V. (2016) Diffusive cation fluxes in deep-sea sediments and insight into the global geochemical cycles of calcium, magnesium, sodium and potassium. *Marine Geology*, **373**, 64–77.

Tang D., Shu X., Ma J., Jiang G., Zhou X. & Shi Q. (2017) Formation of shallow-water glaucony in weakly oxygenated Precambrian ocean: an example from the Mesoproterozoic Tieling Formation in north China. *Precambrian Research*, **294**, 214–229.

Taylor K.G. (1990) Berthierine from the non-marine Wealden (Early Cretaceous) sediments of south-east England. *Clay Minerals*, **25**, 391–399.

Taylor L.L., Quirk J., Thorley R.M.S., Kharecha P.A., Hansen J., Ridgwell A. *et al.* (2016) Enhanced weathering strategies for stabilizing climate and averting ocean acidification. *Nature Climate Change*, **6**, 402–408.

Teng F.-Z., Hu Y., Ma J.-L., Wei G.-J. & Rudnick R.L. (2020) Potassium isotope fractionation during continental weathering and implications for global K isotopic balance. *Geochimica et Cosmochimica Acta*, **278**, 261–271.

Thiry M. & Pletsch, T. (2011) Palygorskite clays in marine sediments: records of extreme climate. *Developments in Clay Science*, **3**, 101–124.

Tilman D., Fargione J., Wolff B., D'Antonio C., Dobson A., Howarth R. *et al.* (2001) Forecasting agriculturally driven global environmental change. *Science*, **292**, 281–284.

Torres M.E., Milliken K.L., Hüpers A., Kim J.-H. & Lee S.-G. (2022) Authigenic clays *versus* carbonate formation as products of marine silicate weathering in the input sequence to the Sumatra Subduction Zone. *Geochemistry, Geophysics, Geosystems*, **23**, e2022GC010338.

Tosca N.J. & Masterson A.L. (2014) Chemical controls on incipient Mg-silicate crystallization at 25°C: implications for early and late diagenesis. *Clay Minerals*, **49**, 165–194.

Tosca N.J. & Tutolo B.M. (2023) Hydrothermal vent fluid–seawater mixing and the origins of Archean iron formation. *Geochimica et Cosmochimica Acta*, **352**, 51–68.

Tosca N.J., Guggenheim S. & Pufahl P.K. (2016) An authigenic origin for Precambrian greenalite: implications for iron formation and the chemistry of ancient seawater. *Geological Society of America Bulletin*, **128**, 511–530.

Tosca N.J., Jiang C.Z., Rasmussen B. & Muhling J. (2019) Products of the iron cycle on the early Earth. *Free Radical Biology and Medicine*, **140**, 138–153.

Tosca N.J., Macdonald F.A., Strauss J.V., Johnston D.T. & Knoll A.H. (2011) Sedimentary talc in Neoproterozoic carbonate successions. *Earth and Planetary Science Letters*, **306**, 11–22.

Tostevin R. & Ahmed I.A.M. (2023) Micronutrient availability in Precambrian oceans controlled by greenalite formation. *Nature Geoscience*, **16**, 1188–1193.

Toth T.A. & Fritz S.J. (1997) An Fe-berthierine from a Cretaceous laterite: part I. Characterization. *Clays and Clay Minerals*, **45**, 564–579.

Tréguer P.J. & De La Rocha C.L. (2013) The world ocean silica cycle. *Annual Review of Marine Science*, **5**, 477–501.

Tréguer P.J., Sutton J.N., Brzezinski M., Charette M.A., Devries T., Dutkiewicz S. *et al.* (2021) Reviews and syntheses: the biogeochemical cycle of silicon in the modern ocean. *Biogeosciences*, **18**, 1269–1289.

United Nations Framework Convention on Climate Change (2015) *Adoption of the Paris Agreement*. Report No. FCCC/CP/2015/L.9/Rev.1. Available at https://unfccc.int/resource/docs/2015/cop21/eng/l09r01.pdf

Vakal S., Yanovska A., Vakal V., Artyukhov A., Shkola V., Yarova T. *et al.* (2020) Minimization of soil pollution as a result of the use of encapsulated mineral fertilizers. *Journal of Ecological Engineering*, **22**, 221–230.

Van der Jagt H., Friese C., Stuut J.-B., Fischer G. & Iversen M.H. (2018) The ballasting effect of Saharan dust deposition on aggregate dynamics and carbon export: aggregation, settling, and scavenging potential of marine snow. *Limnology and Oceanography*, **63**, 1386–1394.

Van Houten F.B. & Arthur M.A. (1989) Temporal patterns among Phanerozoic oolitic ironstones and oceanic anoxia. Pp. 33–49 in: *Phanerozoic Ironstones: An Introduction and Review* (T.P. Young & W.E.G. Taylor, editors). Geological Society of London, London, UK.

Van Houten F.B. & Bhattacharyya D.P. (1982) Phanerozoic oolitic ironstones – geological record and facies models. *Annual Review of Earth and Planetary Sciences*, **10**, 441–457.

Voigt M., Pearce C.R., Fries D.M., Baldermann A. & Oelkers E.H. (2020) Magnesium isotope fractionation during hydrothermal seawater–basalt interaction. *Geochimica et Cosmochimica Acta*, **272**, 21–35.

Vorhies J.S. & Gaines R.R. (2009) Microbial dissolution of clay minerals as a source of iron and silica in marine sediments. *Nature Geoscience*, **2**, 221–225.

Walker J.C., Hays P. & Kasting J.F.A. (1981) A negative feedback mechanism for the long-term stabilization of Earth's surface temperature. *Journal of Geophysical Research: Oceans*, **86**, 9776–9782.

Wallmann K., Aloisi G., Haeckel M., Tishchenko P., Pavlova G., Greinert J. *et al.* (2008) Silicate weathering in anoxic marine sediments. *Geochimica et Cosmochimica Acta*, **72**, 2895–2918.

Wallmann K., Geilert S. & Scholz F. (2023) Chemical alteration of riverine particles in seawater and marine sediments: effects on seawater composition and atmospheric CO_2. *American Journal of Science*, **323**, 7.

Wang C., Konhauser K.O. & Zhang L. (2015) Depositional environment of the Paleoproterozoic Yuanjiacun banded iron formation in Shanxi Province, China. *Economic Geology*, **110**, 1515–1539.

Wang K., Li W., Li S., Tian Z., Koefoed P. & Zheng X.Y. (2021) Geochemistry and cosmochemistry of potassium stable isotopes. *Geochemistry*, **81**, 125786.

Warr L.N. (2020) Recommended abbreviations for the names of clay minerals and associated phases. *Clay Minerals*, **55**, 1–4.

Warr L.N. (2022) Earth's clay mineral inventory and its climate interaction: a quantitative assessment. *Earth Science Reviews*, **234**, 104198.

West A.J., Galy A. & Bickle M. (2005) Tectonic and climatic controls on silicate weathering. *Earth and Planetary Science Letters*, **235**, 211–228.

Wigley R.A. & Compton J.S. (2007) Oligocene to Holocene glauconite phosphorite grains from the Head of the Cape Canyon on the western margin of South Africa. *Deep Sea Research II*, **54**, 1375–1395.

Williams L.B., Hervig R.L. & Hutcheon I. (2001) Boron isotope geochemistry during diagenesis. Part II. Applications to organic-rich sediments. *Geochimica et Cosmochimica Acta*, **65**, 1783–1794.

Wilmsen M. & Bansal U. (2021) Depositional setting and limiting factors of early Late Cretaceous glaucony formation: implications from Cenomanian glauconitic strata (Elbtal Group, Germany). *Facies*, **67**, 24.

Wilson M.J. (1999) The origin and formation of clay minerals in soils: past, present and future perspectives. *Clay Minerals*, **34**, 7–25.

Wilson M.J. (2004) Weathering of the primary rock-forming minerals: processes, products and rates. *Clay Minerals*, **39**, 233–266.

Woltz C.R., Anderson R.P., Tosca N.J. & Porter S.M. (2023) The role of clay minerals in the preservation of Precambrian organic-walled microfossils. *Geobiology*, **21**, 708–724.

Wood B.J. & Kleppa O.J. (1981) Thermochemistry of forsterite-fayalite olivine solutions. *Geochimica et Cosmochimica Acta*, **45**, 529–534.

Xu S., Bufe A., Li S.-L., Erlanger E.D., Ran L., Zhang J. *et al.* (2024) Erosional modulation of the balance between alkalinity and acid generation from rock weathering. *Geochimica et Cosmochimica Acta*, **368**, 126–146.

Yalçin H. & Bozkaya Ö. (2011) Sepiolite-palygorskite occurrences in Turkey. *Developments in Clay Science*, **3**, 175–200.

Yin K., Hong H., Churchman G.J., Li Z. & Fang Q. (2018) Mixed-layer illite-vermiculite as a paleoclimatic indicator in the Pleistocene red soil sediments in Jiujiang, southern China. *Palaeogeography, Palaeoclimatology, Palaeoecology*, **510**, 140–151.

Yin Y.-S., Wei G.-Y., Pogge von Strandmann P.A.E., Lechte M.A., Hohl S.V., Lin Y.-B. *et al.* (2023) Widespread clay authigenesis and highly congruent silicate weathering in the Marinoan aftermath. *Earth and Planetary Science Letters*, **623**, 118423.

Young T.P. (1989) Phanerozoic ironstones: an introduction and review. *Geological Society, London, Special Publications*, **46**, ix–xxv.

Zack T. & Hogmalm K.J. (2016) Laser ablation Rb/Sr dating by online chemical separation of Rb and Sr in an oxygen-filled reaction cell. *Chemical Geology*, **437**, 120–133.

Zhang D., Zhou C.-H., Lin C.-X., Tong D.-S. & Yu W.-H. (2010) Synthesis of clay minerals. *Applied Clay Science*, **50**, 1–11.

Zhang Q., Awolayo A.N., Nightingale M.J. & Tutolo B.M. (2022a) Kinetics of glauconite dissolution in anoxic conditions as a function of pH and temperature. *Geochimica et Cosmochimica Acta*, **336**, 78–91.

Zhang X.Y., Gaillardet J., Barrier L. & Bouchez J. (2022b) Li and Si isotopes reveal authigenic clay formation in a palaeo-delta. *Earth and Planetary Science Letters*, **578**, 117339.

Zheng X.-Y., Beard B.L., Neuman M., Fahnestock M.F., Bryce J.G. & Johnson C.M. (2022) Stable potassium (K) isotope characteristics at mid-ocean ridge hydrothermal vents and its implications for the global K cycle. *Earth and Planetary Science Letters*, **593**, 117653.